


## RESEARCH ARTICLE

# Processing and interpretation of core-electron XPS spectra of complex plasma-treated polyethylene-based surfaces using a theoretical peak model

Marc Bruggeman<sup>1</sup>  | Mischa Zelzer<sup>2</sup> | Hanshan Dong<sup>3</sup> | Artemis Stamboulis<sup>1</sup>

<sup>1</sup>Biomaterials Group, School of Metallurgy and Materials, University of Birmingham, Edgbaston, Birmingham, UK

<sup>2</sup>School of Pharmacy, Biodiscovery Institute, University Park, University of Nottingham, Nottingham, UK

<sup>3</sup>Surface Engineering Group, School of Metallurgy and Materials, University of Birmingham, Birmingham, UK

## Correspondence

Artemis Stamboulis and Marc Bruggeman, Biomaterials Group, School of Metallurgy and Materials, University of Birmingham, Edgbaston, Birmingham B15 2TT, UK. Email: [a.stamboulis@bham.ac.uk](mailto:a.stamboulis@bham.ac.uk) and [mx1082@student.bham.ac.uk](mailto:mx1082@student.bham.ac.uk)

## Funding information

Marie Skłodowska Curie ITN AIMed, Grant/Award Number: 861138; NIHR SRMRC, Grant/Award Number: NIHR SRMRC2

Interpretation of X-ray photoelectron spectroscopy (XPS) spectra of complex material surfaces, such as those obtained after surface plasma treatment of polymers, is confined by the available references. The limited understanding of the chemical surface composition may impact the ability to determine suitable coupling chemistries used for surface decoration or assess surface-related properties like biocompatibility. In this work, XPS is used to investigate the chemical composition of various ultra-high-molecular-weight polyethylene (UHMWPE) surfaces. UHMWPE doped with  $\alpha$ -tocopherol or functionalised by active screen plasma nitriding (ASPN) was investigated as a model system. Subsequently, a more complex combined system obtained by ASPN treatment of  $\alpha$ -tocopherol doped UHMWPE was investigated. Through ab initio orbital calculations and by employing Koopmans' theorem, the core-electron binding energies (CEBEs) were evaluated for a substantial number of possible chemical functionalities positioned on PE-based model structures. The calculated  $\Delta$ CEBEs showed to be in reasonable agreement with experimental reference data. The calculated  $\Delta$ CEBEs were used to develop a material-specific peak model suitable for the interpretation of merged high-resolution C 1 s, N 1 s and O 1 s XPS spectra of PE-based materials. In contrast to conventional peak fitting, the presented approach allowed the distinction of functionality positioning (i.e. centred or end-chain) and evaluation of the long-range effects of the chemical functionalities on the PE carbon backbone. Altogether, a more detailed interpretation of the modified UHMWPE surfaces was achieved whilst reducing the need for manual input and personal bias introduced by the spectral analyst.

## KEYWORDS

ASPN, plasma nitriding, polyethylene, UHMWPE, XPS,  $\alpha$ -tocopherol

**Abbreviations:** ASPN, active screen plasma nitriding;  $\alpha$ T,  $\alpha$ -tocopherol; aTHQ,  $\alpha$ -tocopherylhydroquinone; aTQ,  $\alpha$ -tocopherylquinone; CEBEs, core-electron binding energies; CHPE, the averaged [CH<sub>2</sub>] CEBE of the PE model structure; CH<sub>x</sub>, higher-order carbon shifts due to long-range effects; D/PT, doped and plasma-treated; D/UT, doped and untreated; UD/PT, undoped and plasma-treated; UD/UT, undoped and untreated; UHMWPE, ultra-high-molecular-weight polyethylene.

This is an open access article under the terms of the [Creative Commons Attribution-NonCommercial](https://creativecommons.org/licenses/by-nc/4.0/) License, which permits use, distribution and reproduction in any medium, provided the original work is properly cited and is not used for commercial purposes.

© 2022 The Authors. *Surface and Interface Analysis* published by John Wiley & Sons Ltd.

## 1 | INTRODUCTION

Polyethylene (PE) remains the second most widely used polymer in the past century.<sup>1</sup> Ultra-high-molecular-weight polyethylene (UHMWPE) is predominantly the material of choice for biomedical applications, such as total joint replacements.<sup>2</sup> Over the past decades, various attempts have been made to improve or expand the use of UHMWPE biomaterials including surface modifications.<sup>3–7</sup> Such modifications aim to enhance the mechanical properties and biocompatibility, subsequently improving implant longevity and patient compliance by reducing the chance of implant failure. Plasma treatments are a popular route to alter surface-related properties. Once plasma-treated, the surface often has a complex chemical composition. X-ray photoelectron spectroscopy (XPS) has been shown to be invaluable for the analysis of such surfaces, allowing quantitative chemical characterisation in the upper few nanometres of the material surface.<sup>8</sup>

When investigating materials with few and/or distinct chemical states, XPS spectra interpretation can be relatively straightforward. However, with an increasing number of chemical functionalities present on the surface, peak fitting becomes more complex and potentially prone to personal bias. Generally, when investigating polymeric materials with unknown functionalities, reference data such as provided by Beamson and Briggs and the NIST database are used for comparison.<sup>9,10</sup> However, the subsequent peak fitting applied is limited by the available references and therefore does not always reflect the range of possible functionalities that may form during the surface treatment. Additionally, specifically in the case of the NIST XPS database, a spread in binding energies (BEs) is noted, and this can result in arbitrary spectral interpretation.<sup>11</sup> This is of particular concern in cases where potentially overlapping or unknown chemical functionalities, such as those obtained after surface plasma treatment of polymers, are present.

Using conventional reference databases, the BE assignments used to construct a peak model will originate from various materials. Although some existing reference data can provide a reasonable initial indication for peak assignments, chemical shifts in XPS are dependent on the electronic structure of the investigated molecule(s), and reference data alone can be insufficient for accurate and detailed XPS peak assignment. Specifically, in complex systems where biomolecules are incorporated within the plasma-treated polymer matrices, no suitable literature reference exists. The inability to establish a detailed interpretation of the spectra limits the understanding of the chemical nature of the surface, which may impact the suitability of coupling chemistries used for surface decoration or evaluation of the relation between the chemical surface composition and biomaterial properties like biocompatibility. In such cases, alternative reference sources are desirable to allow a more in-depth interpretation of the experimental XPS spectra.

An extensively applied tool to provide additional reference data for core-electron BE (CEBE) assignments are *ab initio* orbital calculations, which can be performed in various ways using the Hartree–Fock (HF) molecular orbital (MO) theory and density

functional theory (DFT).<sup>12</sup> Although both theories are used to describe the quantum states of many-electron systems, HF MO theory neglects the electron correlation and therefore results in higher energies compared with DFT, which implicitly includes exchange and electron correlation effects.<sup>13,14</sup> A hybrid approach between the two theories also exists, where the exact exchange from the HF theory is ‘hybridised’ with DFT to improve the description of various molecular properties that tend to be poorly described by *ab initio* density functionals.<sup>15,16</sup> The main limitations encountered in such calculations are the required computational effort and the complexity in the subsequent data evaluation. The latter is especially true for those who are not frequent users of computational methods, as in the case of many surface analysts and material scientists. However, due to the development of new and/or more complex material surfaces, the need for CEBE estimation for the interpretation of unidentified spectral features/chemical functionalities increases drastically.

Most literature that utilises calculated CEBEs to interpret experimental XPS spectra make use of simplified model structures, as calculations of solids using periodic conditions as seen in the projected augmented wave (PAW) can be costly and result in the formation of artefacts arising from the periodic unit cells.<sup>12,17</sup> The unrestricted generalised transition-state (uGTS) method was one of the earlier methods to provide accurate absolute BEs for small gas molecules, displaying a mean error of 0.2 eV compared with experimental BEs.<sup>18</sup> Later, it was found that this accuracy was achieved as a result of consistent error cancellation, but it is occasionally still used in the estimation of BEs.<sup>19,20</sup> Other approaches, for example, those employing correlation-consistent basis sets or configuration interaction calculations, display a mean error of around 0.15 eV.<sup>21,22</sup> However, the high computational cost limits their applicability for larger structures and use on ‘average’ PCs.

A more forthright approach for the estimation of CEBEs is using Koopmans’ theorem (KT), where the negative orbital energy ( $-\epsilon_i$ ) is equated to the ionisation potential and thereby provides an estimate for the respective CEBE.<sup>23</sup> KT allows the estimation of CEBEs without calculating the work function, but these CEBEs only include initial state effects as the structure remains in its neutral ground state. KT neglects the electronic relaxation in response to the formed electron core-hole and the CEBEs estimated with KT are therefore also referred to as frozen orbital (FO) CEBEs. Corrections can be applied to absolute CEBEs to account for the relativistic effects and the zero-point energy contribution, but such corrections typically do not influence the CEBE shifts ( $\Delta$ CEBEs) significantly as the errors are small due to error cancellation effects.<sup>12</sup> No differentiation was made between HF orbital energies ( $\epsilon_{\text{HF}}$ ) and Kohn–Sham (KS) orbital energies (i.e. the DFT analogues of HF orbital energies,  $\epsilon_{\text{KS}}$ ), as in both cases, KT is validated in regard to the calculated initial state  $\Delta$ CEBEs.<sup>24</sup> However, contrary to  $\Delta\epsilon_{\text{HF}}$ ,  $\Delta\epsilon_{\text{KS}}$  may not solely be a result of initial state effects due to the exchange and electron correlation effects included with the use of DFT.

The  $\Delta$ CEBEs obtained through KT are shown to allow satisfying spectral interpretation if the energy offset of the calculated CEBEs, relative to the experimental CEBEs, are constant throughout a set of

structures.<sup>25–28</sup> Depending on the method and basis set used for the calculations, the mean error of calculated KT  $\Delta$ CEBEs are typically between 0.2 and 0.7 eV for atoms in the second row of the periodic table when compared with experimental  $\Delta$ CEBEs. This approach is utilised extensively in the literature to aid in the interpretation of various elemental regions, but often focussing on one region at a time and with materials of known chemical composition. However, when working on potentially overlapping and/or unknown functionalities, a single region does not allow for accurate interpretation of the spectra. Instead, it would be desirable to constrain the peak areas of each functionality with all its corresponding components to uphold its theoretical composition during peak fitting to guide the component identification.

As with any XPS peak fitting routine, care has to be taken to avoid data over- and misinterpretation. Recent publications provide a succinct overview of common errors in XPS peak fitting<sup>29,30</sup> and guidance on peak fitting for plasma-treated samples.<sup>31</sup> The theoretical peak model in our approach takes these issues into account and is consistent with all but one of the six points raised in Grecsynski and Hultman's guidelines on XPS data interpretation; namely, (#5) the number of component peaks is not kept to a minimum, although each component in our peak model does have a physical interpretation.<sup>32</sup> Next to that, regarding the other guidelines, (#1) the purpose of the model is formulated, (#2) the model is comprehensive, the model is both (#3) qualitatively and (#4) quantitatively self-consistent, and (#6) uses physically meaningful constraints.<sup>32</sup> However, the very nature of the sample, a complex composition of functionalities with unknown type and quantity of chemical functionalities for which no reference material exists inherently precludes a priori minimisation of the number of component peaks used as would normally be the case in XPS peak fitting. The purpose of this work is to reduce bias in peak assignment of (nitrogen) plasma-treated polymers where conventional approaches relying on reference materials or established reaction pathways of surface modifications are unavailable or fail. For the current system, to be as unbiased as possible with regard to the qualitative assessment of functional groups, we propose that all potential functionalities that may form during the plasma-treatment of PE and subsequent oxidation/ageing of the plasma-treated surface when in contact with air should be considered. It is important to note that we do not propose general use of this unbiased peak fitting approach, but we suggest that its application should only be considered for complex samples that display a large number of different, unpredictable chemical functionalities such as some (not necessarily all) plasma-treated samples.

The present work proposes a self-consistent theoretical peak model suitable for multi-region peak fitting of complex PE-based surfaces that lack suitable reference materials. A  $\Delta$ CEBE database of varying C/N/O functionalities positioned on a PE model structure was generated by ab initio orbital calculations and by employing KT. The calculated  $\Delta$ CEBE database was converted into a multi-region peak model, providing a material-specific solution for the spectral interpretation of merged high-resolution C 1s, N 1s and O 1s XPS spectra. UHMWPE doped with  $\alpha$ -tocopherol or functionalised by active screen

plasma nitriding (ASPN) was investigated as a model system. Subsequently, the use of the KT-based peak model for processing and interpretation of XPS spectra of the more complex, combined system, obtained by ASPN treatment of  $\alpha$ -tocopherol doped UHMWPE was assessed by comparison to conventional peak fitting procedures.

## 2 | MATERIALS AND METHODS

### 2.1 | Computational details

The investigated model structures were based on a 7-mer PE chain (i.e.  $[\text{CH}_2-\text{CH}_2]_7$ ), where functionalities were positioned in the centre (C7 or C8) or at the end of the chain (C1 or C14). Next to the model structures,  $\alpha$ -tocopherol (vitamin E, aT) and two by-products that may form during its antioxidative activity [ $\alpha$ -tocopherylquinone (aTQ) and  $\alpha$ -tocopherylhydroquinone (aTHQ)] were also evaluated (25). All structures were drawn in 'Avogadro' and pre-optimised using the 'Merck Molecular Force Field' (MMFF94) energy minimisation; the coordinates of the pre-optimised structures were used to prepare the input files for the quantum chemistry package 'GAMESS' (v2019. R1.P1.pgiblas).<sup>33,34</sup> Calculations in 'GAMESS' were performed using the 6-311++G(d,p) Pople basis set and the HF method alone or including the long-range and dispersion-corrected hybrid DF wB97X-D.<sup>35,36</sup> The wB97X-D hybrid DF was chosen as it is shown to provide reduced errors in covalent systems compared with more commonly used DFs such as B3LYP-D.<sup>36</sup> It was also demonstrated that self-interaction errors (i.e. the interaction of an electron with itself that results when exchange–correlation contributions to the total energy are approximated, also referred to as delocalisation error) can be greatly reduced by long-range corrected hybrid DFs.<sup>36</sup> This is of importance as self-interacting electrons are observed in core orbitals and the non-bonding regions of valence 1s orbitals (e.g. in hydrogen).<sup>37</sup> The inclusion of a dispersion correction was also found to be beneficial for geometry optimisations, because intramolecular dispersion interactions already affect medium-sized organic molecules.<sup>38</sup> Cartesian basis functions were used to construct the symmetry-adapted linear combination (SALC) of the basis functions, with a linear dependence threshold of 1.0E-6. Second-order SCF orbital optimisation was used for the pure HF calculations, and Pulay's DIIS interpolation was used for the hybrid DFT calculations. The molecular geometries were optimised until they reached a convergence limit of 1.0E-5 with the use of Jacobi diagonalisation. Once completed, the model structures were visualised in 'wxMacMolPlt' to inspect and assign the HF/KS orbital energies to the atoms within the model structures. The orbital energies were assigned to the atom with the highest occupant in the atomic orbital coefficient, that is, the orbital predominantly localised at the atom of interest—for simplicity, from here forth referred to as CEBE. The unrestricted HF (UHF) calculations on the evaluated doublet systems were susceptible to spin contamination; the spin contamination in organic molecules is generally deemed negligible if the total spin ( $\langle S^2 \rangle$ ) deviates less than 10% from  $s(s + 1)$ , where 's' refers to half of the unpaired electrons.<sup>39</sup>

The spin contamination for the carboxylate model structure was shown to be negligible, showing a  $\langle S^2 \rangle$  value of 0.760 and 0.755 as calculated by UHF and WB97X-D, respectively. The spin contamination for the centred and end-chain ammonium ion model structures was also negligible, showing a  $\langle S^2 \rangle$  value of 0.751 as calculated by both methods. Examples of the GAMESS input files are available in the Supporting Information.

## 2.2 | Sample preparation

UHMWPE sheets were purchased at Direct Plastics Ltd (Sheffield, UK) with a thickness of 5 mm. For preparation, the sheets were waterjet cut into squares of  $10 \times 10$  mm and polished. The polishing was performed using silicon carbide grinding papers of 400, 800, 1200 and 2000 grit consecutively for 2 min each, after which finished with a 6- $\mu\text{m}$  diamond polishing paste for an additional 2 min—resulting in undoped and untreated UHMWPE (UHMWPE UD/UT). Prior to any treatment, the samples were washed with ethanol and subsequently left to dry in air at room temperature.  $\alpha$ -Tocopherol was purchased at Sigma-Aldrich Ltd (Dorset, UK) with a purity of 96%. Doping of the polished UHMWPE samples was carried out with fresh  $\alpha$ -tocopherol in a round-bottom flask at 90°C for 4 h under stirring and blanketed with nitrogen—resulting in doped and untreated UHMWPE (UHMWPE D/UT). Plasma nitriding on the undoped and doped UHMWPE surfaces was performed with a 40-kW DC nitriding unit (Klöckner Ionon, Köln, Germany) in combination with an active screen set-up.<sup>40</sup> The active screen mesh cylinder was made of 0.7-mm-thick perforated sheet steel, with an average height of 130 mm and a diameter of 120 mm. The distance between the sample surface and the active screen was set at 20 mm. A gas mixture of 80%  $\text{N}_2$  and 20%  $\text{H}_2$  was used with an initial flow rate of 4 NL/h, after which the vacuum pump was adjusted to balance the pressure at 75 Pa. All treatments were performed at 90°C for a duration of 60 min once the desired temperature was achieved. When completed, the power and inlet gas were switched off so that the plasma chamber was cooled down in the presence of the remaining working gas whilst maintaining the pressure of 75 Pa. When the plasma chamber was cooled down to about 50°C, the vacuum was slowly released, and the samples were removed from the plasma chamber—resulting in undoped plasma-treated and doped plasma-treated UHMWPE (UHMWPE UD/PT and D/PT). The samples were stored in polystyrene Petri dishes and kept in a desiccator for about 2 weeks prior to XPS analysis.

## 2.3 | XPS analysis

XPS spectra were taken at the EPSRC Harwell XPS facility using a Kratos AXIS Supra (Didcot, UK) using a monochromatic Al  $K_{\alpha}$  X-ray source (12 mA  $\times$  12 kV = 144 W). The samples were mounted using a double-sided scotch tape placed on a glass slide and attached using copper clips to the sample bar. The glass slide ensured the samples were floated from the spectrometer. To prevent surface

charge build-up, charge neutralisation was used with a filament current, filament bias voltage, and charge balance voltage of 0.3 A, 4 V, and 4 V, respectively. The base pressure of the spectrometer was  $5 \times 10^{-10}$  Torr, rising to ca.  $1 \times 10^{-9}$  Torr during analysis. Survey spectra were collected in a single sweep at a pass energy of 160 eV, with a dwell time of 100 ms and sweep time of 120 s, using a step size of 1 eV over the energy range of  $-5$ –1200 eV. High-resolution spectra were recorded at a pass energy of 20 eV, with a dwell time of 260 ms and sweep time of 60 s, using a step size of 0.1 eV over an energy window of 23–26 eV, depending on the element. The observed spectral quality and number of sweeps for each of the high-resolution spectra are presented in Table S1. All data was collected at the 'magic angle' (i.e. 54.74°) in the hybrid mode using a slot aperture, resulting in an analysis area of  $700 \times 300$   $\mu\text{m}$ .

## 2.4 | Peak fitting

All peak fitting was performed using CasaXPS (v2.3.24rev1.1B). The high-resolution XPS spectra were corrected manually using the relative transmission function as obtained from the respective VAMAS files of the high-resolution spectra. The relative transmission function needed to be applied manually, as the default transmission correction in CasaXPS is otherwise applied after the user's set area constraints—resulting in the erroneous conversion of peak area between elemental regions. The Kratos RSF library was used to define the area constraints between the respective functionality-related components that were present in the different elemental regions. The peak fitting of the survey spectra was performed using both the 'Shirley' and 'Tougaard' backgrounds in separate data processing procedures, whereas the high-resolution spectra were fitted using the 'Shirley' or 'Polymer U Tougaard'. Both background types were used to investigate the influence of the background type on the observed atomic composition. However, as the survey spectra also contained non-polymeric elements, the choice was made to use the regular 'Tougaard' background instead of the 'Polymer U Tougaard' to allow all elements to be fitted with the same background. Unless stated otherwise, all component peaks were described by the symmetric Voigt-type lineshape LA(1.53,243), the default lineshape in the version of CasaXPS used to perform the presented peak fits. To account for its vibrational structure, the main  $[\text{CH}_{\text{PE}}]$  component representing the  $[\text{CH}_2]_n$  of the unmodified UHMWPE was described by the asymmetric Voigt-type lineshape LA(4.2,9,4)—this lineshape was established by M. C. Biesinger through peak fitting PE and a C18 alkane.<sup>41</sup> The higher-order  $[\text{CH}_2]_n$  carbon shifts,  $[\text{CH}_x]$ , are fitted using the symmetric LA(1.53,243) lineshape, unless stated otherwise. During the high-resolution spectra peak fitting, the component peaks were referenced in position and constrained in FWHM (initial guess: 1 eV; constraint: 0.8–1.8 eV) to a single component per respective elemental region—these may be referred to as 'peak model reference components'. The peak model reference components consist out of  $[\text{CH}_{\text{PE}}]$  within the C 1s region,  $[\text{CNH}_2]$  within the N 1s region and  $[\text{C=O}^*]$  within the O 1s region. The initial position of  $[\text{CH}_{\text{PE}}]$  in the C

1s region, [CNH<sub>2</sub>] in the N 1s region and [C=O\*] in the O 1s region was set to 284.8, 399 and 532 eV, respectively, and were constrained between 282 and 286 eV, 397 and 401 eV and 530 and 534 eV, respectively. Apart from the area% of the contaminants predetermined by the survey spectra, the initial area of all the component peaks in the C 1s region was set to 10E2 and constrained between 0 and 10E6. The area of the component peaks in the other elemental regions was constrained by the respective RSFs and theoretical composition associated with the evaluated functionalities. The peak fits presented in this work were optimised using the 'Levenberg-Marquardt' algorithm as available in CasaXPS. The developed peak models (excluding the sample-specific contaminants) are available upon request; inquiries can be directed to the corresponding authors.

## 3 | RESULTS AND DISCUSSION

### 3.1 | Peak model

#### 3.1.1 | Functionality evaluation

The functionalities considered during peak fitting of nitrogen and/or oxygen plasma-treated polymers vary in the literature but typically include hydroxyl, ether/epoxide, carbonyl, acid/ester, amine, imine, nitrile, amide, and imide functional groups.<sup>5,42–46</sup> However, this is not an exhaustive list of all the possible functionalities because the peak identification, as mentioned previously, is based on comparison with the available reference materials and cannot always provide conclusive results. Furthermore, functionalities showing overlapping/closely positioned BEs are often grouped in the C 1s spectrum (e.g. assigning a single peak between 1 and 1.6 eV above the main hydrocarbon peak to all [C–O/N]-based functionalities) and are most often not further investigated by peak fitting the areas of their corresponding elemental regions. Unfortunately, plasma-polymer surface reactions are not as well understood as pure plasma gas chemistries. Especially in the case of ASPN, where plasma is formed on the active screen instead of directly on the sample, the sample surfaces are mainly subjected to ion bombardment. Consequently, the ion bombardment of the surface can lead to electron-induced fragmentation and low-energy (i.e.  $\leq 50$  eV) electron-induced surface reactions.<sup>47</sup> As ASPN was originally introduced as a treatment for metals, there is also little literature available on ASPN of polymers.<sup>40</sup> Additionally, the available literature focusses on changing surface-related physical/biological properties rather than determining the surface-related chemical changes that have occurred during the ASPN treatment.<sup>5,48</sup> Therefore, a range of additional functionalities were evaluated to encompass more possible functionalities that may have formed during the plasma-chemical reactions—considering the presence of the polymer ([CH<sub>2</sub>]<sub>n</sub>), at least three different gases (oxygen diffused within the polymer and the nitrogen-hydrogen working gas) and two transition metals (Fe and Cr, from the active screen set-up positioned near the sample surface). The complete list

of functionalities, their IDs and additional visual structural information is available in Table S2.

#### 3.1.2 | Peak model assembly

To assemble the calculated peak model that was used during the high-resolution peak fitting, the calculated CEBEs were calibrated over the lowest observed CEBE per model structure, which showed an average of  $304.97 \pm 0.08$  eV as calculated by HF and  $279.45 \pm 0.07$  eV as calculated by wB97X-D ( $\alpha = 0.0001$ ;  $n = 50$ ). From here on, considering UHMWPE chains contain an average of 125,000 to 263,000 [CH<sub>2</sub>] repeating units, all carbon shifts will be considered relative to the averaged [CH<sub>2</sub>] of the PE model structure  $\Delta$ CEBE (i.e. [CH<sub>PE</sub>]) as it is expected to be the most abundant functionality.<sup>49</sup> Examples of various centred and end-chain model structures and their corresponding carbon  $\Delta$ CEBEs are displayed in Figure 1, showing the structural differences in the model structures with an increasing number of non-carbon atoms included. The calculated primary carbon shifts, nitrogen and oxygen shifts and higher-order carbon shifts covering the full PE-based model structures are presented in Tables S3–S5, respectively. On occasion, asymmetry in the estimated  $\Delta$ CEBEs of the PE backbone in model structures with centred functionalities can be observed; this effect is due to long-range effects of the evaluated functionalities and is further discussed in Section 3.1.4. The simplified chemical structures and corresponding  $\Delta$ CEBEs of the tocopherol-like components ([aT], [aTQ] and [aTHQ]) are shown in Table S6.

#### 3.1.3 | Effect of functional group positioning

The effect of the functionality positioning on the calculated  $\Delta$ CEBEs was investigated by taking the difference between the  $\Delta$ CEBEs of end-chain and centred model structures. Within the literature, the effect of functionality positioning is rarely investigated during XPS analysis of modified polymers, and these structural differences are most often grouped during conventional peak fitting despite the clear differences in theoretical composition. Within the Beamson and Briggs reference database, a few experimentally observed  $\Delta$ CEBE deviations due to a difference in functionality positioning were observed. As presented in Table 1, a comparison between the calculated (this work, as available in Table S3) and experimental (Beamson and Briggs reference database)  $\Delta$ CEBEs of esters and carboxylic acids, as well as primary and secondary amides, shows clear differences in the  $\Delta$ CEBEs due to the functionality positioning. Both the calculated and experimental primary carbon  $\Delta$ CEBEs were found to increase when the functionalities were in the end-chain positioning (i.e. carboxylic acid and primary amide) when compared with centred positioning (i.e. ester and secondary amide), showing a  $\Delta$ CEBE increase of roughly 0.30 eV regardless of the functionality. The experimental  $\Delta$ CEBEs showed a slightly higher deviation between the primary and secondary amide positioning when compared with

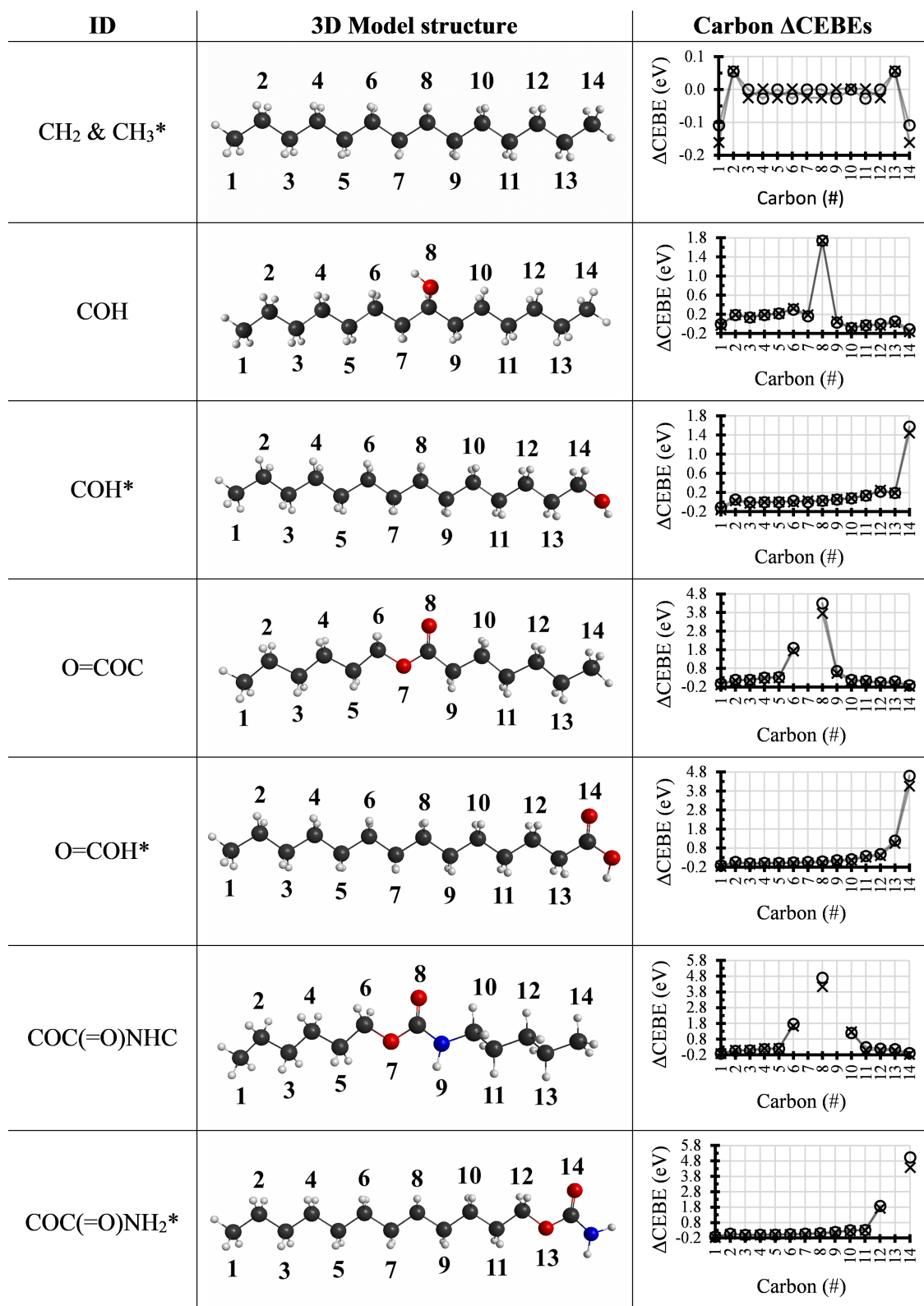


**FIGURE 1** Examples of 3D model structures, showing carbon (black), oxygen (red), nitrogen (blue) and hydrogen (light grey) atoms. The numbers refer to the plotted carbon  $\Delta$ CEBEs relative to [CH<sub>PE</sub>], as calculated by HF (circles) and wB97X-D (crosses).

the calculated  $\Delta$ CEBEs. However, the calculated deviation for this functionality was still within the experimentally observed  $\Delta$ CEBE range. At least one of the calculated  $\Delta$ CEBEs involved in each

functionality exceeds the resolution of state-of-the-art XPS instruments (i.e.  $>0.1$  eV) as shown in Table S7. Therefore, the calculated  $\Delta$ CEBE differences are expected to be significant enough to allow

	HF (eV)		wB97X-D (eV)		Experimental <sup>9</sup> (eV)	
	O=COR	O=CNHR	O=COR	O=CNHR	O=COR	O=CNHR
Centred	4.30	3.41	3.76	2.91	3.99 ± 0.30	3.00 ± 0.02
End-chain	4.60	3.70	4.06	3.21	4.26 ± 0.10	3.45 ± 0.15
$\Delta_{\text{end-centred}}$	0.30	0.29	0.30	0.30	0.27	0.45
$\Delta_{\text{calc-exp}}$	0.03	0.16	0.03	0.15		

Note: 'R' represents the different atom present in the centred or end-chain functionality, C or H, respectively.

**TABLE 1** Comparison between the calculated and mean experimental primary carbon CEBE deviations observed in esters/acids and primary/secondary amides

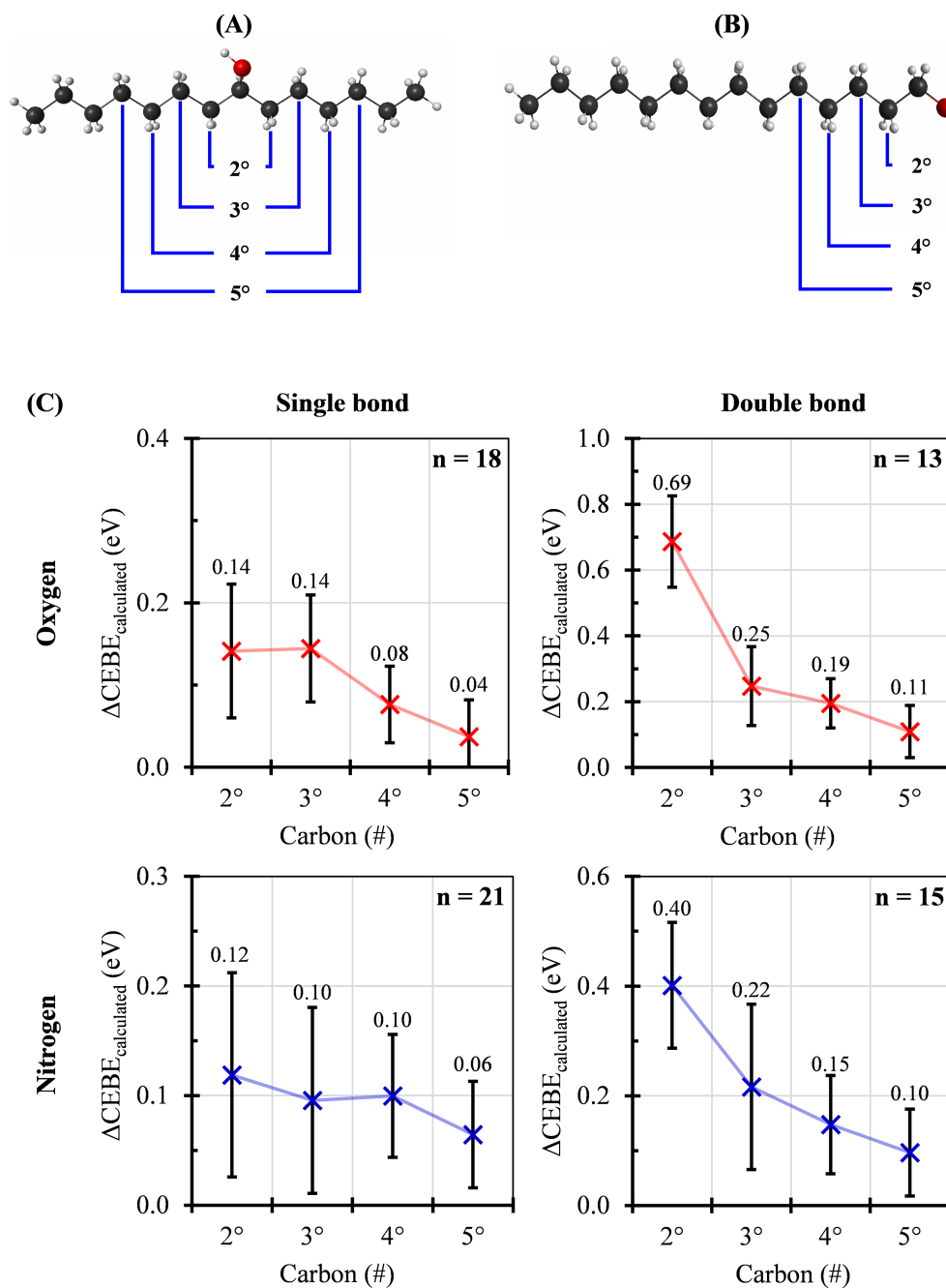


**FIGURE 2** Assignment of higher-order carbon shifts (i.e.  $[\text{CH}_x]$ ) in the centred (A) and end-chain (B) model structures, with the  $[\text{COH}]$  model structure serving as an example. The graphs (C) depict the mean secondary ( $2^\circ$ ,  $x = 1$ ), tertiary ( $3^\circ$ ,  $x = 2$ ), quaternary ( $4^\circ$ ,  $x = 3$ ) and quinary ( $5^\circ$ ,  $x = 4$ )  $\Delta\text{CEBEs}$  for  $[\text{CH}_2]$  groups in the vicinity of carbon-oxygen and carbon-nitrogen functionalities, calculated with 'wB97X-D' relative to  $[\text{CH}_{\text{PE}}]$ . Values are separated by atom type (i.e. oxygen or nitrogen) and bond type (i.e. single or double bond), confidence interval of  $\alpha = 0.01$  with  $n$  as shown per group within the respective graphs.

differentiation between the positioning of functionalities during the high-resolution spectra peak fitting—especially in the case of functionalities with more than one non-carbon atom.

### 3.1.4 | Long-range effects of functional groups

The PE model structures also allowed investigation into the  $\Delta$ CEBEs of neighbouring carbon atoms present in the model structures, which are susceptible to so-called ‘long-range’ effects (i.e. chemical shifts in the XPS spectra due to the presence of a functionality that is not the first nearest neighbour of the functional group under consideration). These long-range effects have been investigated and observed for other polymers, such as TFAA and PVTF. However, to the best of our knowledge, there is a lack of literature on the secondary and higher-order carbon shifts (i.e. BE shifts exerted on carbons that are positioned two or more carbons away from the functionality) as seen in functionalised PE-based material surfaces.

In this work, higher-order carbon shifts are expected to be of importance for several reasons. Excluding this fine structure can result in the erroneous estimation of functionalities, especially those close to the main hydrocarbon peak, such as single-bonded oxygen/nitrogen functionalities. Additionally, by including the higher-order carbon shifts, the theoretical composition of an otherwise unknown chemical surface composition can be estimated during peak fitting (i.e. by constraining the component peak areas by the expected C/N/O ratios of the evaluated functionalities) and component stability (i.e. the observed change in component presence with the inclusion of its associated higher-order carbon shifts) can be evaluated. As ASPN is known for its homogeneous treatment of materials, even in the case of complex geometries/morphologies, an even spatial distribution of the functionalities on the polymer surface was assumed.<sup>5</sup> Using this assumption, increasingly higher-order carbon shifts can be introduced to the peak model until the introduced theoretical composition results in  $[\text{CH}_x]$  overestimation in the C 1s region or underestimation of the components within the N 1s and O 1s regions.

The assignment of the higher-order carbon shifts and the mean influence of carbon–oxygen and carbon–nitrogen functionalities on the  $\Delta$ CEBEs of the PE carbon backbone are shown in Figure 2—separated by atom type and bond type, as calculated by wB97X-D. The mean values calculated by HF are shown in Figure S1, and graphs showing the individual carbon shifts as calculated by HF and wB97X-D per functionality are displayed in Figures S2 and S3, respectively. As the calculated database in this work only contained two model structures containing a carbonyl group, all model structures with double-bonded oxygen are grouped (i.e. carbonyls, esters, and acids). As seen in Figure 2, the secondary carbon shift for single-bonded oxygen is  $\sim 0.14$  eV, for double-bonded oxygen  $\sim 0.69$  eV, for single-bonded nitrogen  $\sim 0.12$  eV and for double-bonded nitrogen  $\sim 0.40$  eV. Typically, the average deviation between the functionalities was roughly  $\pm 0.11$  eV and continuously decreased towards higher-order carbon shifts. It can be clearly observed that double-bonded functionalities influenced the  $\Delta$ CEBEs of  $[\text{CH}_2]$  more than single-bonded functionalities. Additionally, the difference

between the primary and secondary carbon shift was most prominent; this difference decreases considerably when the functional group is situated further away from the primary carbon. Around the quinary carbon shift, most functionalities showed no significant ( $\leq 0.1$  eV) long-range effects on the  $\Delta$ CEBEs of the PE carbon backbone. Within the reference database of Beamson and Briggs, only four mean secondary carbon shifts were reported that relate to oxygen-based functionalities.<sup>9</sup> The reported secondary carbon shift for single-bonded oxygen was  $\sim 0.2$  eV, for carbonyl oxygen  $\sim 0.4$  eV and for ester/acid-like functionalities  $\sim 0.4$  to  $\sim 0.7$  eV. The mean calculated and experimental oxygen-based secondary carbon  $\Delta$ CEBEs are similar although not identical. Differences in the  $\Delta$ CEBEs were also most likely affected by energy referencing/material-specific differences. It is worth to note the higher-order carbon shifts can be small (as shown in Figure 2, for 3° or above typically  $< 0.30$  eV) and within the range of experimental errors of around 0.20–0.30 eV, but only through their inclusion the self-consistency of the peak model can be maintained. The inclusion of the higher-order carbon shifts should reduce the erroneous estimation of functionalities close to the hydrocarbon peak during high-resolution peak fitting.

In the present work, the higher-order carbon shifts were introduced as individual component peaks per respective functionality during peak fitting. This was done to maintain the stoichiometry of the present elements and to account for the occasional asymmetry observed in the carbon  $\Delta$ CEBEs of the PE backbone in the model structures with centred functionalities as was observed in Figure 1. The observed charge distribution in the model structures, which are clearly asymmetrically affected by the orientation of the centred functional groups in cases such as  $[\text{COH}]$  but symmetric in cases such as  $[\text{COC}_\alpha]$  and  $[\text{C=O}]$ , gives rise to inequivalent or equivalent carbon sites, respectively. The origin of the asymmetry in the  $\Delta$ CEBEs of the PE backbone can be illustrated by the 2D molecular electrostatic potential contour maps of the model structures; examples of  $[\text{COH}]$ ,  $[\text{COC}_\alpha]$  and  $[\text{C=O}]$  are depicted in Figure S4. This shows that despite the alkyl segments on both sides of the centred functionality are chemically equivalent, electrostatic effects introduced by the functionalities impact the observed  $\Delta$ CEBEs in the carbon backbone and are dependent on the orientation of the functionality. The influence of electrostatic effects arising from chemical functionalities positioned in hydrocarbon backbones was reported in the literature for molecules in a self-assembled monolayer theoretically and experimentally.<sup>51,52</sup> In this work, it was shown that functional groups exert long-range effects on the alkyl segments regardless of chain length, which resulted in asymmetry in the CEBEs of the carbons in the alkyl segments.<sup>51,52</sup> This work highlighted that electrostatic effects significantly contribute to the shifts observed in CEBEs, which is in agreement with our observations.<sup>51</sup>

### 3.1.5 | Comparison and validation of peak models

To assess the peak model quality, the calculated  $\Delta$ CEBEs and experimental  $\Delta$ CEBEs from the Beamson and Briggs database are compared



by linear correlation.<sup>9</sup> A difficulty in the comparison of calculated  $\Delta$ CEBEs versus experimental  $\Delta$ CEBEs is introduced by energy referencing. When comparing the same material of a known composition that displays a XPS spectrum with a clear separation of components, energy referencing the C1s region has little to no impact on the relative shifts. However, this is not valid when the aliphatic hydrocarbon peak cannot be clearly identified, as is the case with complex samples where introduced functionalities have peak positions near the aliphatic hydrocarbon peak (e.g. C–O/N) as is frequently observed in the literature of plasma-treated polymers.<sup>5,42–46</sup> Within the reference database, the XPS spectra for aliphatic polymers are calibrated to 285 eV, but this neglects the fact that different polymers may have a difference in their C 1s region

maximum. Because of this, energy referencing can result in data misinterpretation and has received substantiated criticism over the past decades.<sup>11</sup> Furthermore, averaged experimental  $\Delta$ CEBEs are used for the assignment of functional groups, most of which originate from various materials and occasionally show relatively large material-specific deviations in their  $\Delta$ CEBE.

To allow one-to-one comparison, the  $\Delta$ CEBEs in the linear correlations are compared from the lowest experimental CEBE available per respective region—the hydrocarbon in the C 1s region, the secondary amine in the N 1s region and the secondary amide in the O 1s region. The linear correlation graphs and corresponding statistical analysis are displayed in Figure 3 and Table 2, respectively. The origin of the experimental reference data within the Beams on

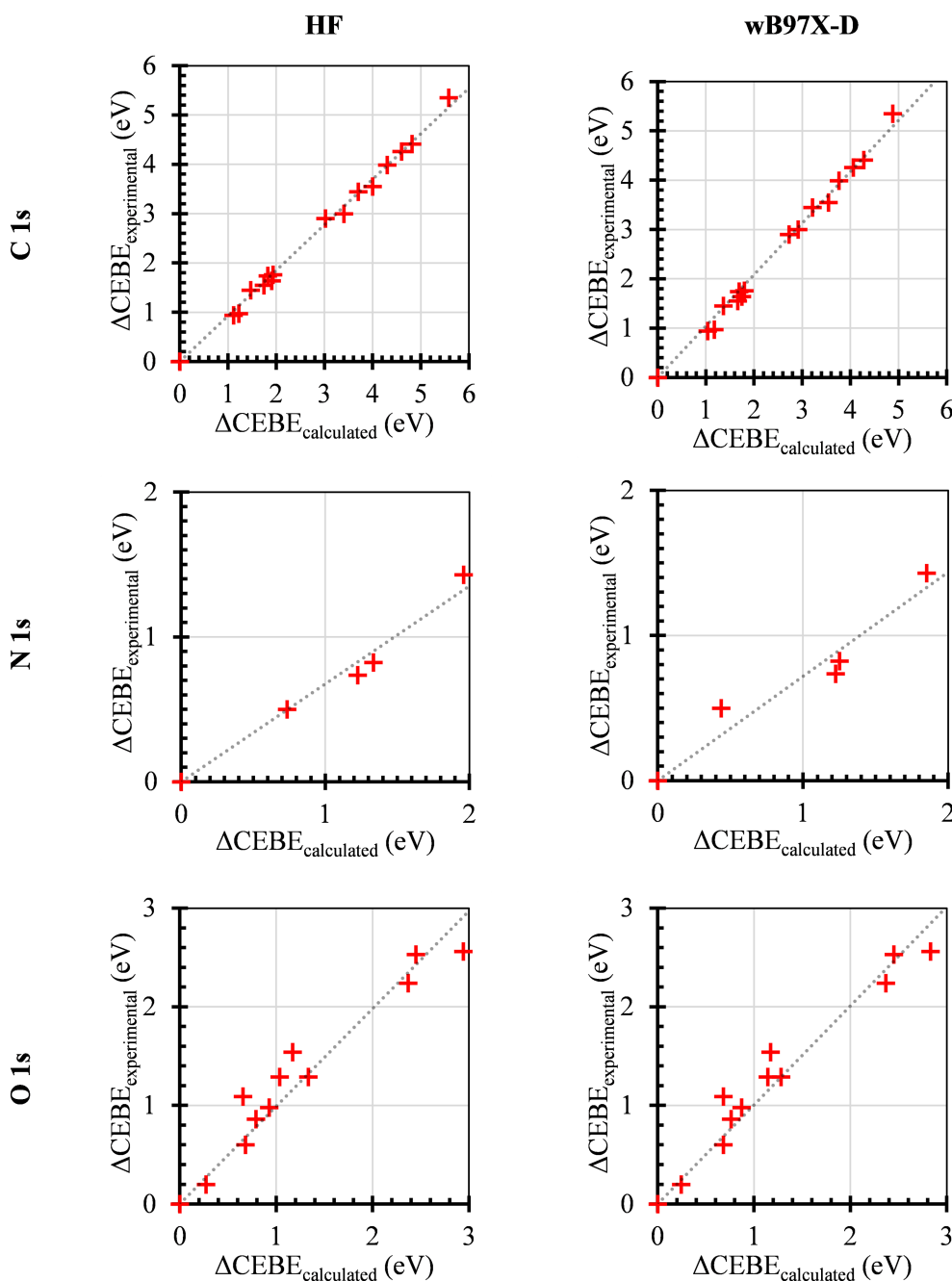


**FIGURE 3** Linear correlation fits of the HF (left) and wB97X-D (right) calculated  $\Delta$ CEBEs versus the experimental  $\Delta$ CEBEs, relative to the lowest experimental CEBE per elemental region. The C 1s values are relative to the hydrocarbon, the N 1s shifts are relative to the centred secondary amine, and the O 1s shifts are relative to the centred secondary amide

**TABLE 2** Statistical analysis showing the slope (a), offset (b) and regression coefficient ( $R^2$ ) of the linear fits, as well as the Pearson correlation coefficient ( $r_p$ ), the mean absolute error (MAE), and the maximum absolute deviation (MAX) between the experimental and calculated  $\Delta$ CEBE datasets

		Slope (a)	Offset (b; eV)	$R^2$	$r_p$	MAE (eV)	MAX (eV)
HF	C 1s	0.92	20.07	1.00	1.00	0.22	0.45
	N 1s	0.68	23.53	0.99	0.99	0.36	0.53
	O 1s	0.99	26.28	0.98	0.97	0.16	0.44
wB97X-D	C 1s	1.04	-5.39	1.00	1.00	0.14	0.48
	N 1s	0.72	-6.86	0.97	0.97	0.30	0.49
	O 1s	1.01	-9.11	0.98	0.98	0.15	0.41

and Briggs database is shown in Table S8. The individual ( $\Delta$ )CEBEs per functionality as used in the linear correlation fits are shown in Tables S9–S11.

The C 1s  $\Delta$ CEBEs are reasonably well estimated by HF, but the linear correlation is notably improved after the introduction of wB97X-D with a reduction of the mean absolute error from 0.22 to 0.14 eV. The observed mean absolute error and maximum absolute error when involving DFT in this work (0.14 and 0.48 eV, respectively) showed to be smaller than those observed in the simulated C 1s spectra of organic monolayers by Giesbers et al (0.30 and 0.67 eV, respectively; compared with the average error based on the methods that used a Pople basis set).<sup>25</sup> A direct comparison with the C 1s simulated spectra of Giesbers et al was also performed; the observed differences in the estimated  $\Delta$ CEBEs compared with this work are shown in Table S12.<sup>25</sup> The mean absolute difference of the C 1s  $\Delta$ CEBEs between this work and the work of Giesbers et al is 0.2 and 0.1 eV for HF and wB97X-D, respectively.<sup>25</sup> There are methodological and structural differences between this work and the work of Giesbers et al (Giesbers et al used a smaller basis set, different DF and silicon clusters, whereas this work made use of a PE backbone), and the values provided by Giesbers et al were only available up to the first decimal place, limiting the extent to which conclusions can be drawn. The calculated N 1s  $\Delta$ CEBEs are overestimated by both HF and wB97X-D when compared with the experimental N 1s  $\Delta$ CEBEs and showed an increased mean absolute error of 0.36 and 0.30 eV, respectively. Compared with our results, almost identical errors in calculated N 1s CEBEs are reported in the literature, where organic monolayers on silicon and metal-based model structures were investigated, although the literature values show a linear correlation that is closer to unity when compared to our work.<sup>25,53</sup> The N 1s CEBEs estimated by Zuilhof et al (using B3LYP/6-311+G(d,p)) showed a mean absolute error of 0.40 eV and a maximum absolute error of 0.54 eV, whereas Zhao et al (also using B3LYP/6-311+G(d,p)) showed a mean absolute error of 0.27 eV and maximum absolute error of 0.67 eV. Both above-mentioned articles made use of the commercially available package ‘natural bond orbital (NBO) analysis’ to estimate CEBEs. This was not included in this work with the intent to keep our method free of charge. The similarity of the mean absolute errors between the estimated and experimental CEBEs in our work and that reported in the literature shows the quality of estimation to be comparable. Zuilhof et al and Zhao et al compared their estimated CEBEs to experimental data acquired at various laboratories including their own for their small-molecule-based monolayers. This work solely

compared the calculated CEBEs with the Beamson and Briggs polymer database, as this database is built from data acquired from polymer-based samples, which is more appropriate for our PE-based surfaces. Lastly, the observed mean absolute error in the O 1s region is relatively small, showing an error of 0.16 eV with HF and 0.15 eV with wB97X-D.

Altogether, a comparison of the calculated  $\Delta$ CEBEs to the mean experimental  $\Delta$ CEBEs indicated a strong correlation. Both methods demonstrated a regression coefficient ( $R^2$ ) and a Pearson correlation coefficient ( $r_p$ ) of 0.97 or higher for all the investigated regions, indicating that the experimental and calculated values linearly correlate with each other. The overestimation of the  $\Delta$ CEBEs in the N 1s region as observed by the linear correlation slope is noted as a concern. However, this error may be (partially) introduced by energy referencing/material-specific differences. Despite that, the calculated  $\Delta$ CEBEs are in reasonable agreement to the experimental  $\Delta$ CEBEs, with those obtained by wB97X-D consistently exhibiting a lower error compared with those obtained by HF. Therefore, the wB97X-D-based peak model was used during the high-resolution peak fitting.

## 3.2 | XPS analysis

### 3.2.1 | Survey XPS spectra

The XPS survey spectra of the various UHMWPE samples are available in Figure S5, showing the polymer undoped and untreated (A; UD/UT), undoped and plasma-treated (B; UD/PT), doped and untreated (C; D/UT) and doped and plasma-treated (D; D/PT). The region maxima after energy referencing the C 1s region maximum to 284.8 eV (to allow comparison with the literature) are presented in Table S13. To quantify the elemental regions, both the ‘Shirley’ and the ‘Tougaard’ background were used, in separate data processing procedures, to inspect the change in the atomic composition due to the choice of background, as shown in Table 3. Generally, the deviations in the observed atomic composition due to the change in the background are small apart from iron (more specifically, Fe 2p). The results from the survey spectra needed to perform the high-resolution peak fitting are discussed below; a more in-depth discussion on the survey spectra peak fits and the rational on contaminant assignments is available in the Supporting Information.

For the identification of the contaminants and their contributions to the C 1s and O 1s peak fits into account, reference BE tables were

**TABLE 3** Atomic composition of UHMWPE UD/UT (A1-3), UD/PT (B1-3), D/UT (C1-3) and D/PT (D1-3), determined by the survey spectra fitted with a Shirley/(Tougaard) background

	Atomic concentration ± St. dev. (%)			
	C 1s	N 1s	O 1s	Contaminants
A1	91.46 ± 0.07 (91.59 ± 0.08)	0.64 ± 0.05 (0.50 ± 0.07)	5.92 ± 0.04 (5.94 ± 0.03)	Si 2p 1.72 ± 0.02 (1.67 ± 0.02) F 1s 0.27 ± 0.03 (0.31 ± 0.04)
A2	98.24 ± 0.05 (98.33 ± 0.07)	-	1.76 ± 0.05 (1.67 ± 0.07)	-
A3	89.20 ± 0.05 (89.14 ± 0.11)	0.83 ± 0.03 (0.88 ± 0.11)	7.74 ± 0.04 (7.72 ± 0.04)	Si 2p 2.23 ± 0.03 (2.25 ± 0.02)
B1	64.28 ± 0.10 (61.56 ± 0.09)	15.55 ± 0.09 (16.15 ± 0.08)	16.42 ± 0.07 (16.86 ± 0.07)	Fe 2p 2.10 ± 0.05 (3.63 ± 0.03) Cr 2p 0.98 ± 0.03 (1.40 ± 0.03) Mo 3d 0.08 ± 0.01 (0.06 ± 0.01) Na 1s 0.32 ± 0.03 (0.18 ± 0.02) Cl 2p 0.27 ± 0.01 (0.16 ± 0.01)
B2	64.50 ± 0.09 (61.98 ± 0.07)	16.37 ± 0.08 (16.39 ± 0.07)	16.28 ± 0.05 (16.34 ± 0.06)	Fe 2p 1.34 ± 0.06 (3.50 ± 0.03) Cr 2p 1.03 ± 0.03 (1.37 ± 0.03) Mo 3d 0.07 ± 0.01 (0.06 ± 0.01) Na 1s 0.23 ± 0.02 (0.22 ± 0.02) Cl 2p 0.19 ± 0.01 (0.15 ± 0.01)
B3	84.39 ± 0.07 (83.88 ± 0.07)	5.47 ± 0.06 (5.79 ± 0.07)	9.66 ± 0.04 (9.86 ± 0.05)	Si 2p 0.49 ± 0.02 (0.47 ± 0.02)
C1	90.55 ± 0.05 (90.61 ± 0.05)	-	6.03 ± 0.04 (6.09 ± 0.04)	F 1s 2.75 ± 0.03 (2.61 ± 0.04) Si 2p 0.66 ± 0.02 (0.69 ± 0.02)
C2	90.91 ± 0.06 (90.83 ± 0.06)	-	6.50 ± 0.05 (6.64 ± 0.05)	Si 2p 2.18 ± 0.03 (2.11 ± 0.03) Al 2p 0.41 ± 0.01 (0.42 ± 0.02)
C3	95.38 ± 0.08 (95.27 ± 0.08)	-	4.11 ± 0.08 (4.40 ± 0.07)	Si 2p 0.51 ± 0.02 (0.34 ± 0.02)
D1	77.59 ± 0.09 (77.01 ± 0.09)	11.00 ± 0.08 (11.36 ± 0.08)	11.41 ± 0.06 (11.63 ± 0.06)	D1-3 <sup>a</sup>
D2	79.90 ± 0.08 (79.45 ± 0.07)	10.42 ± 0.08 (10.88 ± 0.06)	9.68 ± 0.04 (9.67 ± 0.04)	Fe 2p 0.32 ± 0.02 (0.34 ± 0.02)
D3	81.55 ± 0.08 (81.20 ± 0.08)	8.95 ± 0.07 (9.06 ± 0.07)	9.50 ± 0.05 (9.73 ± 0.05)	Cr 2p 0.33 ± 0.01 (0.36 ± 0.01)

<sup>a</sup>Averaged presence as determined in the summed spectrum; intensity too low in individual spectra to determine component area.

prepared based on the data available in the NIST database.<sup>10</sup> The BEs used to identify the minor contaminants (i.e. fluoride, chloride, sodium and aluminium) are shown in Table S14. The major contaminants (i.e. silicon, chromium and iron) were evaluated using more extensive BE tables, as shown in Tables S15–S17, respectively. Lastly, where applicable, the corresponding oxygen and nitrogen BEs of the contaminants are presented separately in Table S18. Next to assigning the most likely components based on the observed region maxima, the major contaminants are also investigated by means of peak fitting. The survey spectra peak fits of the Si 2p, Cr 2p<sub>(3/2)</sub> and Fe 2p<sub>(3/2)</sub> regions are presented in Figures S6–S8, respectively. The observed component concentrations of the fits are depicted in Figures S9–S11, respectively; these are also tabulated per peak fit individually in Tables S19 and S20.

In preparation for the high-resolution peak fitting, a conversion table was prepared to account for the expected presence of the silicon- and metal-based contaminants in the high-resolution spectra as determined by the survey peak fits, available in Tables S21 and S22, respectively. To allow conversion, the components are assumed to uphold their assigned theoretical composition. As it was uncertain

if the constrained or unconstrained survey peak fits were more accurate, an average of the respective peak fits was used to estimate the contaminant species present within each region. It was expected that this would introduce the least amount of error, considering the different survey peak fits identified the same components, albeit in somewhat different quantities. The conversion tables contain those that will be included in the high-resolution fits, apart from an unidentified fluoride-based component in 'C1' and aluminium identified as Al<sub>2</sub>O<sub>3</sub> in 'C2'—which is expected to make up  $([0.41 \text{ At } \%_{\text{Al}2\text{p}} \cdot \frac{3}{2}] / 6.50 \text{ At } \%_{\text{O}1\text{s}} = )$  9.46 area% of the 'C2' its O 1s region.

### 3.2.2 | High-resolution XPS spectra

The high-resolution XPS spectra of UHMWPE UD/UT (A1-3), UD/PT (B13), D/UT (C1-3) and D/PT (D1-3) are available in Figure S12. The C 1s region maximum was referenced to 284.8 eV to allow comparison of the peak positions to the literature. Both the 'Shirley' and the 'Universal Polymer Tougaard' background were used, in separate data processing procedures, to fit the high-resolution spectra to inspect

the difference in the atomic composition due to the background change as shown in Table S23. After introducing the peaks associated with the contaminants, constraining their position as determined by the BE reference tables and constraining their area% as was established by the survey spectra peak fits, the high-resolution spectra were fitted using the peak model as calculated by wB97X-D. One of the UHMWPE-based high-resolution spectra fitted using the 'Shirley' background was selected from each of the sample series, namely, 'A2' (as it was the least oxidised/contaminated UHMWPE reference sample), 'B1', 'C3' (as it indicated the presence of  $\alpha$ -tocopheryl quinone, [aTQ], similarly to 'D1-3') and 'D1'.

The tables depicting the component concentrations (pre-determined contaminants established with the survey spectra were omitted) as obtained from the individual high-resolution peak fits of UHMWPE UD/UT (A1-3), UD/PT (B1-3), D/UT (C1-3) and D/PT (D1-3) using a 'Shirley' background and the wB97X-D-based peak model including the respective higher-order carbon shifts are presented in Tables S24–S27. When comparing the component tables, it can be observed that the introduction of the higher-order carbon shifts had minimal effect on the type of functionalities identified by the peak model, but it does influence the estimated presence or positioning (i.e. centred or end-chain). This is due to the positional constraints set for the peak model reference components (see Section 2.4), as the peak models could move freely within the set BE ranges per elemental region, the influence of energy referencing in terms of component identification is prevented (as the  $\Delta$ CEBEs relative to the peak model reference component remain constrained). As shown in Figure S13, energy referencing still introduced a deviation in the observed absolute CEBEs between sample series (A, B, etc.). It was observed that the untreated samples (A and C) showed the [CH<sub>PE</sub>] component at about 284.7 eV, whereas the plasma-treated samples (B and D) showed the [CH<sub>PE</sub>] component at about 284.5 eV—this may be caused by the C1s region maximum shifting upwards as the newly introduced functionalities form photoelectron peaks close to the main hydrocarbon peak. Apart from samples series 'B1-3', the peak model reference components in the showed a similar positioning between the samples of the same series (D1, D2, etc.).

The high-resolution peak fits of the UHMWPE UD/UT and D/UT samples ('A2' and 'C3') allowed a reasonable fit of the C 1s region using the LA(4.2,9,4) lineshape for the [CH<sub>PE</sub>] peak model reference component, as presented in Figures S14 and S15, respectively. The introduction of the higher-order carbon shifts had negligible influence on the peak fits of 'A2'; only a small improvement in the residual standard deviation (STD) was noted from 1.747 to 1.634—which was expected considering the low degree of oxidation components that are associated with the higher-order carbon shifts. A minor [ $\pi - \pi^*$ ] presence was observed in the C 1s region of 'A2', likely due to some contamination originating from the polystyrene Petri dishes used for sample storage—which was accounted for by introducing an additional position-constrained component to the peak model between 291 and 292 eV. Based on ATR-FTIR peak fits of UHMWPE D/UT, the expected presence of the tocopherol-like components is between 9% and 22%

as shown in Figure S16. It is worth to note that the sampling depth of ATR-FTIR (several microns) is much higher than for XPS (several nanometres), making it difficult to compare the observed chemical composition between these two techniques. However, the estimation of the tocopherol-like components present in the polymer matrix is necessary to guide the model when overestimation of the tocopherol-like components is expected. The introduction of the higher-order carbon shifts to 'C3' only slightly increased the presence of [aTQ]; when comparing the composition observed with the 1° and 4° carbon peak model, it increased from 14.9%<sub>[aTQ]</sub> to about 17.7%<sub>[aTQ]</sub>, respectively; the estimated presence of the tocopherol-like components matches closely to that observed by ATR-FTIR (ranging from 9% to 22%). Further addition of the higher order carbon shifts had a negligible impact on the composition as seen in Table S26, indicating the peak model reached a 'stable' component estimation.

From the peak fits of UHMWPE UD/PT (B1-3), it was established that the wB97X-D-based peak model including the 3° carbon shifts was most suitable for fitting the high-resolution XPS spectra of the plasma-treated UHMWPE surfaces evaluated in this work. As can be observed in the fitted spectra of 'B1' shown in Figure S17, the introduction of the higher-order carbon shifts improved the residual STD of the spectra fits from 1.671 to 1.492 until the introduction of the 4° carbon shifts (residual STD = 3.311); Following the incorporation of the 4° carbon shifts, the peak model suffered from [CH<sub>2</sub>] overestimation in the C 1s region and underestimation of the components within the N 1s and O 1s regions. This also indicates that, although lineshapes designed from unmodified polymers are suitable to fit their reference spectra, a single unconstrained asymmetric peak is not sufficient to estimate the hydrocarbon presence in the modified PE-based surfaces due to the long-range effects arising from the newly introduced functional groups affecting the [CH<sub>2</sub>]  $\Delta$ CEBEs of the polymer backbone. It is thought that the increase of the C 1s region FWHM, as observed in Figure S12, forced the [CH<sub>PE</sub>] peak to broaden (average FWHM<sub>[CH]</sub> in A13 was 1.07 eV; average FWHM<sub>C1s</sub> in B1-3 was 1.17 eV) and resulted in increased tailing towards higher BEs with the asymmetric lineshape used for the [CH<sub>PE</sub>] component peak.

The high-resolution peak fits of the combined system, UHMWPE D/PT (D1), using the higher-order carbon shift models are presented in Figure 4 and its corresponding component graph in Figure 5. Using the ATR-FTIR peak fits discussed previously (showing 9%–22% tocopherol-like products) and the UHMWPE D/UT (C3) model system (showing ~78% [CH<sub>PE/x</sub>] and ~16% tocopherol-like products), the presence of the tocopherol-like components in the high-resolution peak fits of 'D1' using the 1° carbon peak model appeared drastically overestimated (showing ~19% [CH<sub>PE/x</sub>] and ~44% tocopherol-like products). When comparing the high-resolution spectra of sample series 'C' and 'D' in Figure S12, this overestimation was expected to be the result of spectral broadening introduced after plasma-treatment of doped UHMWPE. The broadened spectra made it more complicated for the 1° and 2° carbon peak models to distinguish between the [CH<sub>PE/x</sub>] associated with the UHMWPE carbon backbone or the tocopherol-like components. The inclusion of the

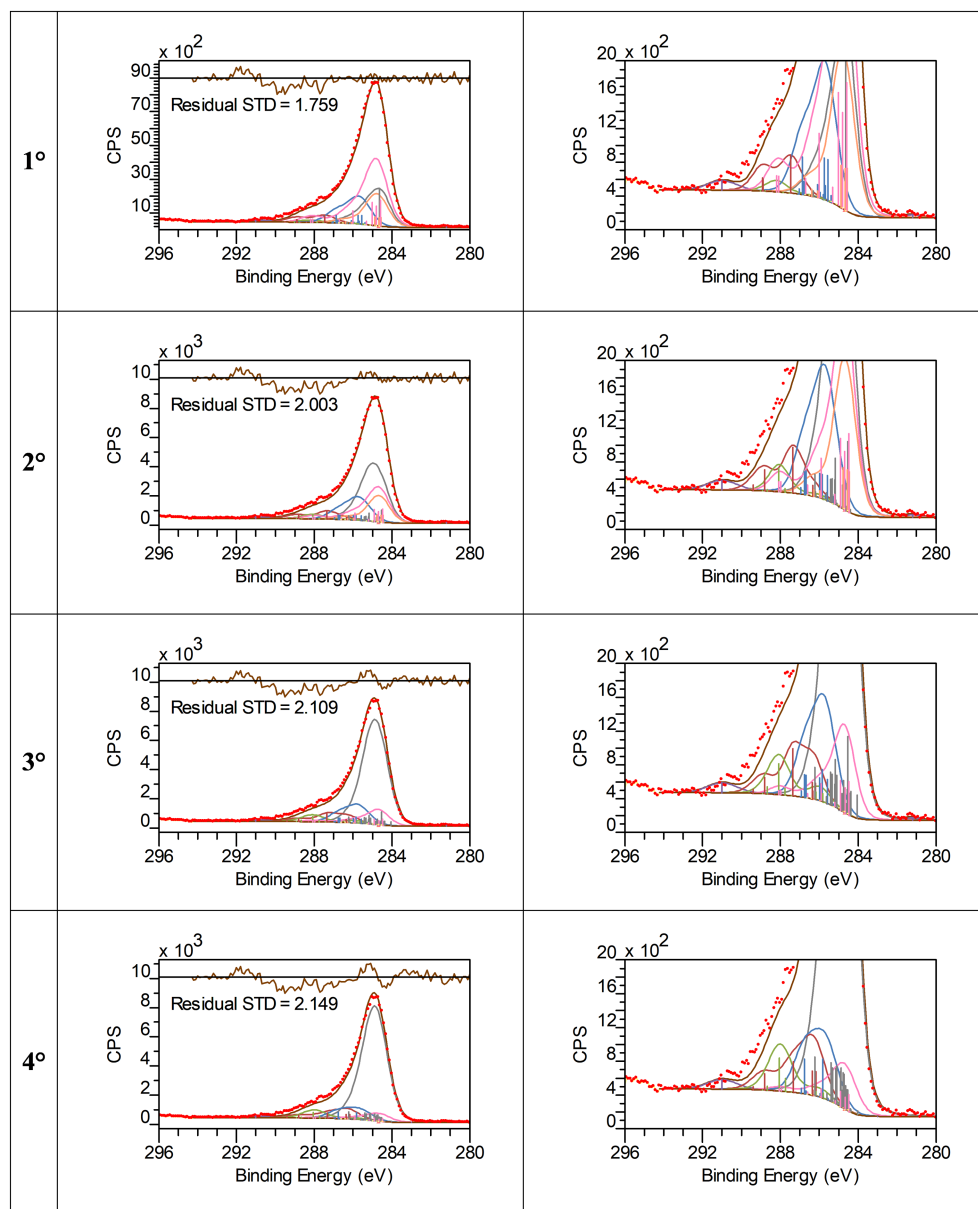


**FIGURE 4** High-resolution C 1s spectra peak fits of UHMWPE D/PT (D1) using a ‘Shirley’ background and the wB97X-D-based peak model including the respective higher-order carbon shifts. The spectra display the recorded experimental data (red, dotted) and the summed peak model envelope (brown, solid). The colours represent the various component groups: [CH] (grey), [CO] (dark red), [CN] (blue), [CNO] (green), [aT] (orange), [aTQ] (pink), [aTHQ] (yellow) and contaminants (purple)

higher-order carbon shifts forced the reduction of the tocopherol-like components, but the peak model consistently identified [aTQ] throughout the peak fits. Similarly, as it was established during the peak fitting of UHMWPE UD/PT (B1), the 3° carbon peak model seemed most suitable for fitting the high-resolution XPS spectra of the UHMWPE D/PT surfaces evaluated in this work. As it can be observed in Figure 4, most of the residual area is situated at the higher BEs (288–291 eV) in the C 1s region and may be a result of unresolved loss events, neglected peak asymmetry or a minor error in the RSFs used as peak area constraints between the elemental regions—as Kratos RSFs are related to homogeneous materials, which excludes homogeneous materials with surface contamination. The high-resolution peak fit of ‘D1’ using the 3° carbon peak model is presented in more detail with labelling in Figure 6. The peak fits indicated that the inclusion of the higher-order carbon shifts prevented

the overestimation of the tocopherol-like components incorporated within the polymer matrix.

The component graph of the high-resolution peak fits, displaying the observed component concentrations of the above-discussed samples’ high-resolution peak fits (i.e. ‘A2’, ‘B1’, ‘C3’ and ‘D1’) using the 3° carbon peak model, is shown in Figure 7. As it can be observed in the component graph, the components identified by the peak model in the combined system (UHMWPE D/PT) generally agree to those identified from the respective model systems (UHMWPE UD/UT, UD/PT and D/UT). The high-resolution peak fits of the untreated reference samples, UHMWPE UD/UT (A2) and D/UT (C3), both showed the presence of [C=O\*]. However, only the peak fit of UHMWPE UD/UT (A2) showed some minor additional oxidation products (i.e. [O=COH\*] and [O=COC=O]), and UHMWPE D/UT (C3) showed the presence of [aTQ]. When comparing the high-resolution peak fits

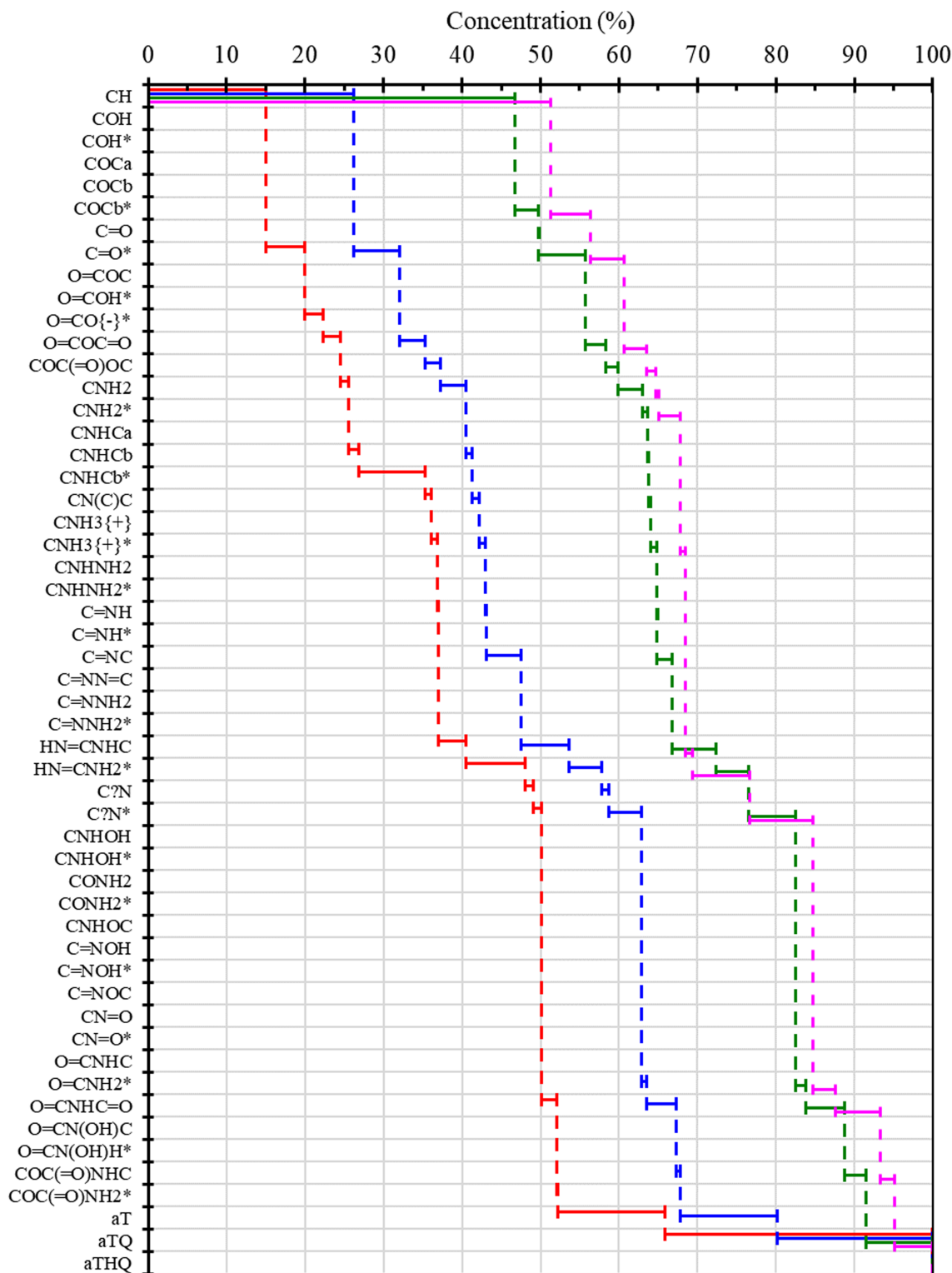


**FIGURE 5** Composition of UHMWPE D/PT (D1) determined by the high-resolution spectra peak fits using a ‘Shirley’ background and the wB97X-D-based peak model including the 1° (red), 2° (blue), 3° (green) and 4° (pink) higher-order carbon shifts. The bars depict the component presence, stacking up to a total of 100%

of the functionality-rich samples obtained after ASPN treatment of the reference samples, UHMWPE UD/PT (B1) and D/PT (D1), the presence of [C=O\*], [O=COC=O], [CNH<sub>2</sub><sup>(\*)</sup>], [O=CNH<sub>2</sub>\*] [O=CNHC=O] and [HN=CNHR] were observed in both plasma-

treated sample series – where ‘R’ represents the atom present in the centred or end-chain functionality, C or H, respectively. However, only the peak fit of UHMWPE UD/PT (B1) showed the presence of [CNH<sub>2</sub>NH<sub>2</sub>\*] and [C=NH\*], and only with UHMWPE D/PT (D1) the

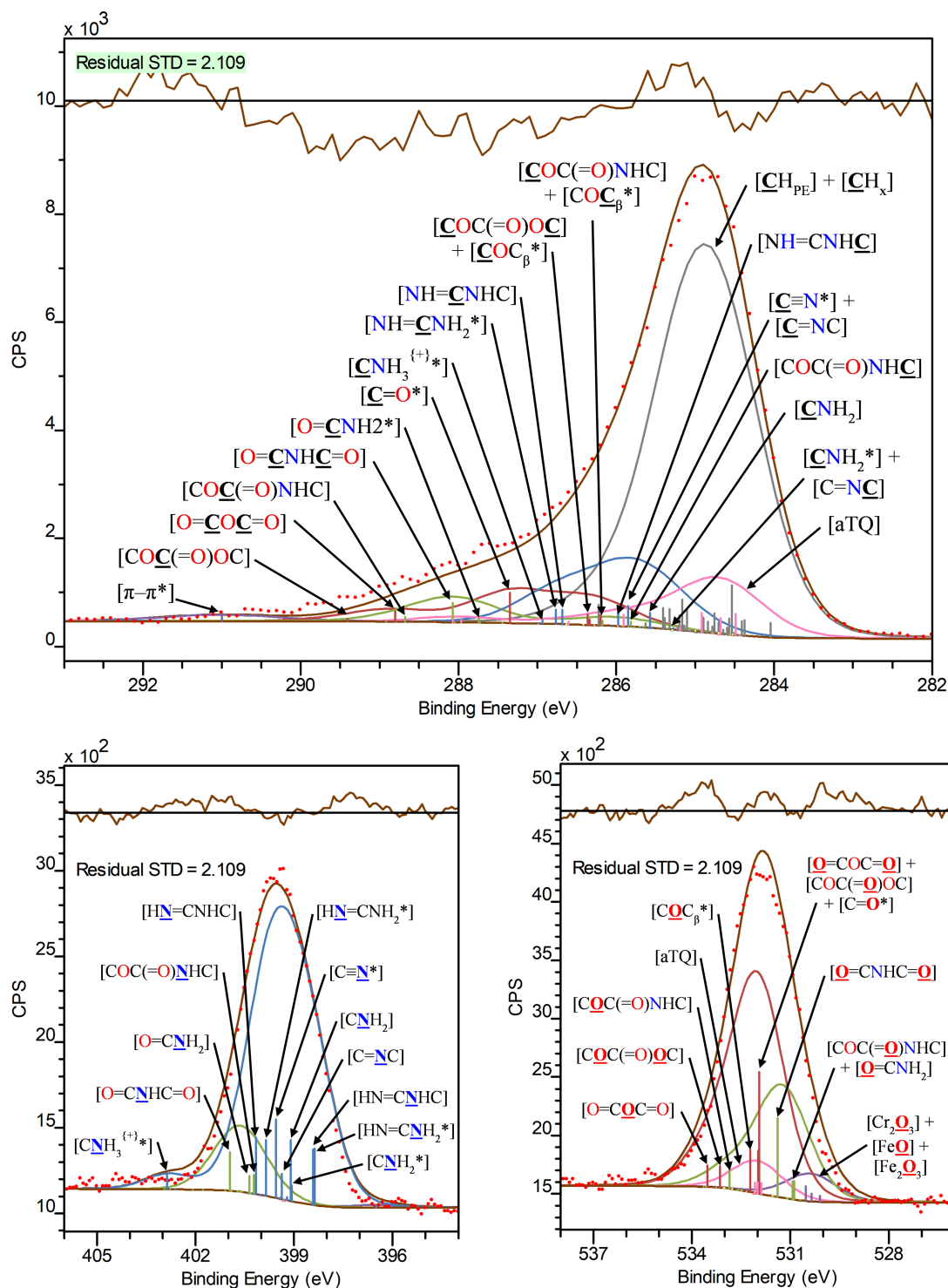


**FIGURE 6** High-resolution C 1s, N 1s and O 1s spectra peak fit of UHMWPE D/PT (D1) using a ‘Shirley’ background and the wB97X-D peak model with the 3<sup>rd</sup> higher-order carbon shifts. The spectra display the experimental data (red, dotted) and the summed peak model envelope (brown, solid). The colours represent the various component groups: [CH] (grey), [CO] (dark red), [CN] (blue), [CNO] (green), [aTQ] (pink) and contaminants (purple). The labels denote the component IDs, with the evaluated atom **bold** and underlined

presence of  $[\underline{\text{C}}\underline{\equiv}\underline{\text{N}}^*]$  was noted. As it can be observed in Tables S23–S26, the components identified in the ‘B’ sample series correspond more often to functionalities in their end-chain positioning when the samples also showed metal contamination (i.e. Fe and Cr) in their

corresponding survey spectra (i.e. ‘B1’ and ‘B2’; see Section 3.2.1). But the samples showing little to no sign of metal contamination (i.e. ‘B3’ and ‘D1-3’) predominantly showed the presence of functionalities in their centred positioning.

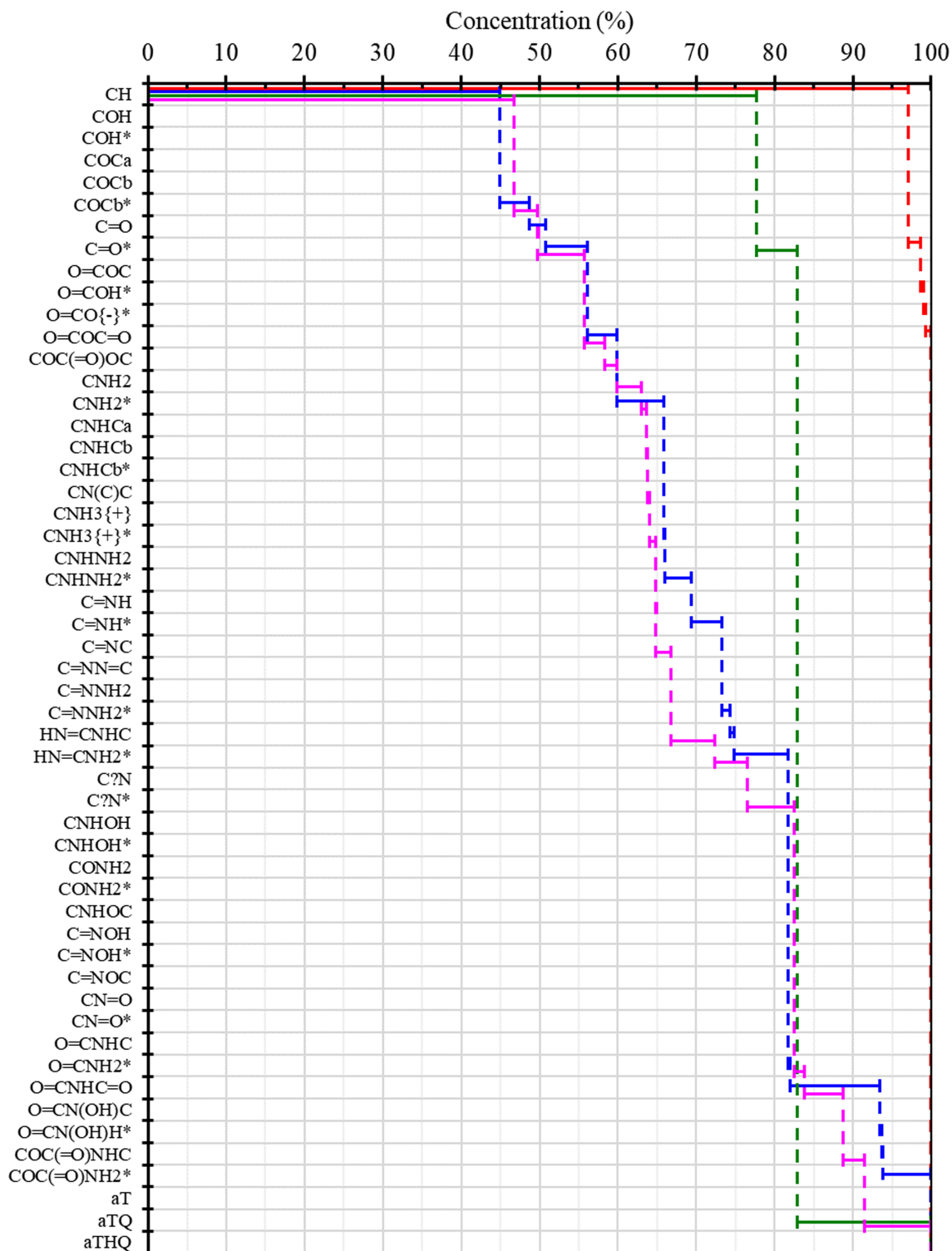


**FIGURE 7** Composition of UHMWPE UD/UT (A2, red), UD/PT (B1, blue), D/UT (C3, green) and D/PT (D1, pink), determined by the high-resolution spectra peak fits using a ‘Shirley’ background and the wB97X-D-based peak model including the 3° higher-order carbon shifts. The bars depict the component presence, stacking up to a total of 100%

The high-resolution spectra of selected samples (i.e. ‘B1’ and ‘D1’) were also further investigated by using the ‘Universal Polymer Tougaard’ background during peak fitting with the 3° carbon peak model to observe the difference in peak model response due to a

change in background. In addition to that, the use of the asymmetric lineshape LA(4.2,9,4) was also tested for all [CH<sub>x</sub>] components instead of solely for the [CH<sub>PE</sub>] component to investigate the influence of increased peak asymmetry on the peak model response. As presented



in Figure S19, the change in the background and peak asymmetry had a negligible impact on most component with the peak fits of 'B1' and 'D1' when using the 3<sup>o</sup> carbon peak model. When using the asymmetric lineshape for the higher-order [CH<sub>x</sub>] components, only minor variation is observed in the presence of some components. The peak fits involving 'B1' showed a maximum average deviation of 2.55 At% for [COC(=O)NH<sub>2</sub>\*]. The peak fits involving 'D1' showed a maximum average deviation of 4.98 At% for [αT] and 4.58 At% for [CH]; the [αT] component was only present in the fits including the asymmetric higher-order [CH<sub>x</sub>] components. The minimal changes observed when changing the background type or introducing peak asymmetry indicate that the peak model is robust, especially in terms of component identification.

### 3.2.3 | Comparison with reference-based peak fitting

To demonstrate the improved detail that was achieved when using the developed multi-region peak model for the interpretation of the complex system (UHMWPE D/PT, D1), a comparison was made with (i) conventional reference-based peak fitting (i.e. area-unconstrained peak fitting of the C 1s region; informed but not computationally connected to the N 1s and O 1s regions) and (ii) advanced reference-based peak fitting (i.e. area-constrained multi-region peak fitting of the C 1s, N 1s and O 1s regions). The C 1s spectra peak fits of the comparison between the various peak fitting approaches are presented in Figure 8. The corresponding N 1s and O 1s spectra peak

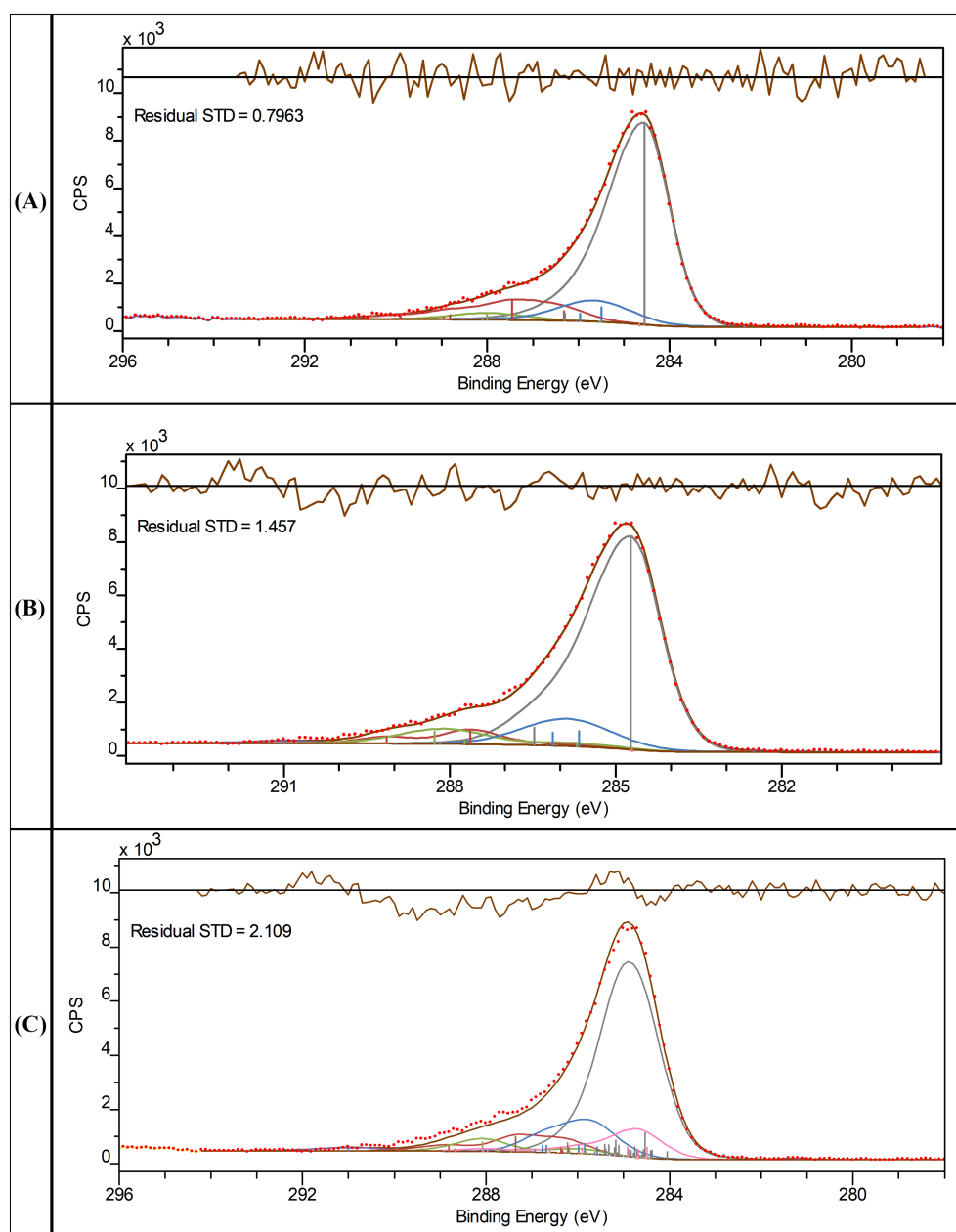


**FIGURE 8** High-resolution C 1s spectra peak fits of UHMWPE D/PT (D1) using a 'Shirley' background following conventional reference-based peak fitting (A), advanced reference-based peak fitting (B) and the wB97X-D-based peak fitting using the 3<sup>o</sup> higher-order carbon shifts (C). The spectra display the experimental data (red, dotted) and the summed peak model envelope (brown, solid). The colours represent the various component groups: [CH] (grey), [CO] (dark red), [CN] (blue), [CNO] (green), [αTQ] (pink) and contaminants (purple)

fits are shown in Figure S20. Positional constraints were based on the mean  $\Delta$ CEBEs from the Beamson and Briggs database as used in the linear correlations, available in Tables S9–S11. With the reference-based peak fitting (i and ii), the considered functionalities were those typically seen with the XPS spectral interpretation of plasma-treated polymeric surfaces.<sup>5,42–46</sup> The evaluated functionalities and chemical compositions as obtained after peak fitting are tabulated in Table 4; the components that showed no presence after peak fitting using the wB97X-D-based peak model were omitted for readability but are depicted in Table S27.

With the conventional reference-based peak fitting, a C 1s region peak model was used to identify the present components. The observed presence of the components was informed by the observed peak shifts and magnitude of the peak ratios of the corresponding

peak fits of the N 1s and O 1s regions. However, as the peak areas of the components within each elemental region are unconstrained, the peak fits are individual least-square solutions and therefore hard to control—often resulting in subjective interpretation due to manual influence from the spectral analyst. Nonetheless, as it can be observed in the N 1s and O 1s peak fits of the conventional reference-based peak fits in Figure S20, both regions were fitted with three components. The N 1s region is fitted with a component to reflect carbon single-bonded nitrogen ([C–NX]), carbon triple-bonded nitrogen ([C $\equiv$ N]) and oxygen double-bonded to a carbon single-bonded nitrogen ([O=C–N]), whereas the corresponding O 1s region was fitted with components presenting carbon single-bonded oxygen ([C–OX]), carbon double-bonded oxygen ([C=O]) and oxygen double-bonded to a carbon single-bonded nitrogen ([O=C–N]). Altogether, this minimal

**TABLE 4** Composition of the high-resolution spectra peak fits of UHMWPE D/PT (D1) using a ‘Shirley’ background following (a) conventional peak fitting, (b) reference-based advanced peak fitting and (c) wB97X-D-based peak fitting using the 3<sup>rd</sup> higher-order carbon shifts

ID	A (At%)	B (At%)	ID	C (At%)
CH	57.5	59.9	CH	46.7
C–OX	0.00	0.91	COC <sub><math>\beta</math></sub> *	3.06
C=O	8.97	5.59	C=O	0.04
			C=O*	5.95
O=COC	2.85	0.02	O=COC	0.00
O=COH*	1.16	0.00	O=COH*	0.00
O=COC=O	0.95	3.15	O=COC=O	2.60
COC(=O)OC	7.06	0.22	COC(=O)OC	1.57
C–NX	9.56	9.31	CNH <sub>2</sub>	3.04
			CNH <sub>2</sub> *	1.57
			CNHC <sub><math>\beta</math></sub>	0.04
			CN(C)C	0.34
			CNH <sub>3</sub> <sup>f(+)*</sup>	0.69
C=N or HN=C–NX	Not evaluated		C=NC	1.93
			HN=CNHC	5.66
			HN=CNH <sub>2</sub> *	4.19
C $\equiv$ N	5.07	7.95	C $\equiv$ N*	5.96
O=CNHC	1.15	3.66	O=CNHC	0.00
O=CNH <sub>2</sub> *	5.26	0.00	O=CNH <sub>2</sub> *	1.31
O=CNHC=O	0.50	9.28	O=CNHC=O	4.84
COC(=O)NHC	Not evaluated.		COC(=O)NHC	2.75
aTQ	Not evaluated.		aTQ	8.55
ID	A (At%)	B (At%)	C (At%)	
CH	57.5	59.9	55.2	
CO	21.0	9.90	13.2	
CN	14.6	17.3	22.6	
CNO	6.91	12.9	8.90	

Notes: Presenting the individual component presence (based on the combined presence of all corresponding atoms related to the respective IDs) and the summed presence of the various component groups as grouped in the peak fits: [CH], [CO], [CN] and [CNO]. For ease of comparison, the atomic composition determined with the conventional reference-based peak fitting of the C 1s region (a), was adjusted to reflect the inclusion of the corresponding [N and O] atoms. Additionally, as the reference-based peak fitting did not include the tocopherol-like components, the summed [CH] presence in ‘C’ represents the combined presence of [CH] and [aTQ].

interpretation of the N 1s and O 1s provides sufficient rationale to consider the major functionalities that are typically peak fitted with plasma-treated polymeric surfaces to the C 1s region peak model.<sup>5,42–46</sup> The subsequent peak fit of the C 1s region, where effort was made for the peak fit to reflect the peak ratios of the above-discussed components fitted within the N 1s and O 1s regions, showed a major presence (>5%) of [C=O], [COC(=O)OC], [C–NX], [C≡N] and [O=CNH<sub>2</sub>].

Despite that the conventional reference-based peak fitting provided strong indications of the present component groups (i.e. [C–OX], [C–NX], [O=C–N], etc.), the area-unconstrained peak fits do not provide a detailed interpretation, remain hard to control and are prone to arbitrary interpretation. Therefore, advanced reference-based peak fitting was also explored, where a reference-based multi-region peak model was used to interpret the merged high-resolution spectra. Similarly, as with the high-resolution peak fitting performed using the developed peak model in Section 3.2.2, the areas of the component peaks in the N 1s and O 1s regions were constrained to the C 1s region components with the respective RSFs and theoretical composition associated with the evaluated functionalities. In contrast to the area-unconstrained reference-based peak fit, a significantly larger presence of [O=CNHC=O] is noted instead of [O=CNH<sub>2</sub>\*]. The presence of the [CO] components showed a decrease from 21.0% to 9.90%, the [CN] components showed an increase from 14.6% to 17.3%, and the [CNO] components showed an increase from 6.91% to 12.9% between the reference-based area-unconstrained and multi-region peak fits, respectively.

Altogether, little change was observed in the [CH] presence, and the main interplay of the component's presence was noted between the other component groups: [CO], [CN] and [CNO]. The main difference observed when switching from the reference-based multi-region peak model (Model B) to the developed multi-region peak model (Model C) was an increase in [CO] and [CN], most likely because significantly more nitrogen-based functionalities were evaluated, which were not included within the Beamson and Briggs database. However, despite the inclusion of the additional functionalities in the developed peak model, various similarities between the reference-based and developed multi-region peak fits were also recognised. For example, both multi-region peak fits showed a notable presence of [C=O], [C≡N] and [O=CNHC=O]. However, where the reference-based peak fit showed a major presence of [C–NX], this seemed to have shifted in the wB97X-D-based peak fit to the newly introduced [HN=CNHR] components—where 'R' represents the atom present in the centred or end-chain functionality, C or H, respectively. The inclusion of the carbon double-bonded nitrogen functionalities with the developed peak model increased the presence of nitrogen and reduced that of [O=CNHC=O] compared with the reference-based multi-region peak fit.

The residual STD increased when comparing the conventional reference-based peak fitting with the advanced reference-based peak fitting and with the wB97X-D-based peak fitting (0.7963, 1.457 and 2.109, respectively), which was to be expected as the peak model became increasingly more constrained. Most of the residual in both

the reference-based and developed multi-region peak models was noted at the higher BEs in the C 1s region (i.e. 288–291 eV) and likely a result of unresolved loss events, neglected peak asymmetry or a minor error in the RSFs used as peak area constraints between the elemental regions (as RSFs are related to homogeneous materials, which excludes homogeneous materials with surface contamination). However, as was observed with the reference-based peak fits, it was difficult to identify functionalities that extend outside the reference database. More specifically, various functionalities that contain more than one  $\Delta$ CBE within an elemental region (i.e. amidine, carbamate, etc.) were seldomly evaluated within the reference database—limiting the ability of detailed spectral interpretation. This is where conventional peak fitting becomes more subjective when involving other references or prone to personal experience or bias in terms of component identification.

Another difficulty of using the conventional reference database to construct a peak model for the interpretation of complex, high-resolution XPS spectra arises from the fact that the observed  $\Delta$ CBEs will originate from a variety of materials. As a result of the latter, common evaluated component groups such as [C–NX] display broad BE ranges (>0.8 eV) in the reference database. Additionally, as discussed in Section 3.2.2, there are indications that energy referencing the C 1s region maximum to 284.8 eV is not suitable when comparing the XPS spectra of the unmodified and modified UHMWPE surfaces—as the functionalities closely positioned to the main hydrocarbon peak influence the C 1s region maximum. However, contrary to reference-based peak fitting, this issue was resolved by using the developed multi-region peak model and with positional constraints for the peak model reference components (see Section 2.4) that are flexible enough to overcome the influence of the functionalities near the main hydrocarbon peak.

Using conventional peak fitting, the typical generalisations observed to improve peak fitting convenience (e.g. assigning a single peak to describe all [C–O]/[C–N]-based functionalities, or grouping differences in functionality positioning despite the variation in the theoretical composition of, e.g. centred and end-chain functionalities) limit the ability to establish a detailed spectral interpretation. As was shown previously in Section 3.1.3, a comparison of the calculated  $\Delta$ CBE database to the experimental  $\Delta$ CBEs showed that the deviation introduced by the change in functionality positioning is significant enough to allow differentiation during the high-resolution XPS spectra peak fitting. Ultimately, the developed approach allowed the identification of a small number of functional groups (out of a larger number of possible functionalities) whose presence could not readily be predicted or 'guessed' otherwise using conventional XPS peak fitting. Biomolecules incorporated within the polymer matrix were able to be distinguished by the peak model—which was not possible with reference-based peak fitting due to a lack of available references in the literature.

Furthermore, as the long-range effects of the evaluated functionalities on the carbon backbone are not considered with reference-based peak fitting, component stability (i.e. the observed change in component presence with the inclusion of its associated higher-order

carbon shifts) cannot be evaluated through spectral processing. When peak fitting functionality-rich polymeric surfaces, such as those obtained after plasma treatment of polymers, peak fitting based on the nearest neighbour analysis is insufficient to establish the full hydrocarbon presence and may result in data misinterpretation. Instead, using the higher-order carbon shifts included within the developed peak model, the theoretical composition of the otherwise unknown chemical surface composition can be estimated during peak fitting (i.e. by the area constraints set on the component peaks with the respective RSFs and theoretical composition of the evaluated functionalities).

As with any theoretical model, there are limitations to the peak model due to its highly constrained nature, the observed outcome may deviate if a different method was used to estimate the ( $\Delta$ )CEBEs or the positional and/or FWHM constraints were set differently/relaxed. Furthermore, in the present work, vibrational and configurational effects on the  $\Delta$ CEBEs are neglected. However, the developed peak model provides a material-specific solution for PE-based surfaces and highly reproducible peak fits. Based on comparison with the reference-based peak fitting and the fact that many if not most of the components included in the developed peak model had peak areas at or close to zero indicates that the model and data are able to handle the input of functionalities in the model that are, or are not, present on the surface. Manual input and personal bias (in terms of component identification) from the spectral analyst becomes negligible—apart from when establishing the presence of contaminants and setting the positional constraints of the peak model reference components.

## 4 | CONCLUSIONS

This work presents a systematic investigation on PE-based model structures using *ab initio* orbital calculations and by employing KT. The calculated orbital energies served as CEBE estimates to develop a material-specific peak model, which is used for the multi-region spectral interpretation of complex C 1s, N 1s and O 1s XPS spectra of UHMWPE. The PE model structures provided a sensible reproduction of the expected chemical environments of the evaluated functionalities whilst keeping the computational effort to a minimum to evaluate a substantial number of chemical functionalities. The calculated  $\Delta$ CEBEs, which allowed comparison to experimental  $\Delta$ CEBEs of the Beamson and Briggs reference database, showed a strong linear correlation and were in reasonable agreement. Using the calculated  $\Delta$ CEBE database and developed peak models, various effects influencing the core-level XPS spectra of PE were able to be investigated.

The calculated  $\Delta$ CEBE database provides insight into significantly more chemical functionalities than those available within conventional reference databases. It was shown that energy referencing the C 1s region is most likely not suitable when comparing the XPS spectra of the unmodified and modified UHMWPE surfaces and may lead to data misinterpretation. The developed peak model allowed for the

separation of the functionalities that are typically grouped together for peak fitting convenience, as well as their positioning (i.e. centred or end-chain). Additionally, the developed peak model allowed for the distinction of biomolecules incorporated within the polymer, which would not have been possible with the use of reference-based peak fitting. Erroneous estimation of the chemical functionalities near the main hydrocarbon peak was reduced by introducing the higher-order carbon shifts. This further indicated that typical nearest neighbour analysis, as observed in reference-based peak fitting, is insufficient to establish the hydrocarbon presence of the UHMWPE carbon backbone. The developed multi-region peak model, which is constrained by the respective RSFs and theoretical composition associated with the evaluated functionalities, provided a robust framework to interpret the XPS spectra of complex PE-based surfaces in more detail than possible with advanced reference-based peak fitting. It is expected that the developed multi-region peak model is transferable to other plasma-treated PE-based systems.

## ACKNOWLEDGEMENTS

All authors would like to thank Dr Mark Isaacs, for the acquisition of the XPS data at the EPSRC HarwellXPS facility. M.B. would like to thank the School of Metallurgy and Materials at the University of Birmingham for providing a studentship. M.B. and A.S. would also like to thank the NIHR SRMRC at the University of Birmingham as well as the Marie Skłodowska Curie ITN AIMed under the grant agreement 861138 for providing further funding.

## AUTHOR CONTRIBUTIONS

M.B. devised the main conceptual ideas, carried out the sample preparation and orbital calculations and assembled the developed peak models. M.B. and M.Z. were in charge of spectral interpretation, processed the data and performed the data analysis. M.B. and M.Z. took the lead in writing the manuscript in consultation with A.S. A.S. and H.D. supervised different parts of the project.

## DATA AVAILABILITY STATEMENT

The data that supports the findings of this study are available in the supplementary material of this article.

## ORCID

Marc Bruggeman  <https://orcid.org/0000-0001-8523-2545>

## REFERENCES

- Richardson J. Polyethylene versus polypropylene: Expect the unexpected. 2018. <https://www.icis.com/asian-chemical-connections/2018/09/polyethylene-versus-polypropylene-expect-the-unexpected/>
- Kurtz S. *UHMWPE biomaterials handbook: Ultra high molecular weight polyethylene in total joint replacement and medical devices*. Academic Press; 2009.
- Zhang M, James SP, King R, Beauregard G. Surface modification of UHMWPE for use in total joint replacements. *Biomed Sci Instrum*. 2004;40:13-17.
- Cho EH, Lee SG, Kim JK. Surface modification of UHMWPE with  $\gamma$ -ray radiation for improving interfacial bonding strength with bone

- cement (III). *Curr Appl Phys.* 2005;5(5):475-479. doi:10.1016/j.cap.2005.01.013
5. Kaklamani G, Mehrban N, Chen J, et al. Effect of plasma surface modification on the biocompatibility of UHMWPE. *Biomed Mater.* 2010;5(5):054102. doi:10.1088/1748-6041/5/5/054102
6. Riveiro A, Soto R, del Val J, et al. Laser surface modification of ultra-high-molecular-weight polyethylene (UHMWPE) for biomedical applications. *Appl Surf Sci.* 2014;302:236-242. doi:10.1016/j.apsusc.2014.02.130
7. Manoj Kumar R, Halder S, Rajesh K, Ghosh S, Lahiri D. Comparative study on the efficacy of the UHMWPE surface modification by chemical etching and electrostatic spraying method for drug release by orthopedic implants. *Mater Sci Eng C.* 2019;105:110117. doi:10.1016/j.msec.2019.110117
8. Briggs D. *Surface analysis of polymers by XPS and static SIMS.* Cambridge University Press; 1998. doi:10.1017/CBO9780511525261
9. Beamson G, Briggs D. *High resolution XPS of organic polymers. Sci ESCA 300 database.* Chichester: John Wiley & Sons; 1992.
10. Naumkin AV, Kraut-Vass A, Gaarenstroom SW, Powell CJ. NIST X-ray photoelectron spectroscopy database, NIST Standard Reference Database Number 20, National Institute of Standards and Technology, Gaithersburg MD, 20899 (2000), doi:10.18434/T4T88K.
11. Greczynski G, Hultman L. Compromising science by ignorant instrument calibration—Need to revisit half a century of published XPS data. *Angew Chem Int ed.* 2020;59(13):5002-5006. doi:10.1002/anie.201916000
12. Viñes F, Sousa C, Illas F. On the prediction of core level binding energies in molecules, surfaces and solids. *Phys Chem Chem Phys.* 2018;20(13):8403-8410. doi:10.1039/c7cp08503f
13. Hollister C, Sinanoglu O. Molecular binding energies. *J Am Chem Soc.* 1966;88(1):13-21. doi:10.1021/ja00953a003
14. Amusia MY, Msezane AZ, Shaginyan VR. Density functional theory versus the Hartree-Fock method: Comparative assessment. *Phys Scr.* 2003;68(6):C133-C140. doi:10.1238/Physica.Regular.068aC0133
15. Becke AD. A new mixing of Hartree-Fock and local density-functional theories. *J Chem Phys.* 1993;98(2):1372-1377. doi:10.1063/1.464304
16. Perdew JP, Ernzerhof M, Burke K. Rationale for mixing exact exchange with density functional approximations. *J Chem Phys.* 1996;105(22):9982-9985. doi:10.1063/1.472933
17. Schwerdtfeger P. The pseudopotential approximation in electronic structure theory. *ChemPhysChem.* 2011;12(17):3143-3155. doi:10.1002/cphc.201100387
18. Chong DP. Accurate calculation of core-electron binding energies by the density-functional method. *Chem Phys Lett.* 1995;232(5):486-490. doi:10.1016/0009-2614(94)01378-9
19. Endo K, Shimada S, Kato N, Ida T. Analysis of valence XPS and AES of (PP, P4VP, PVME, PPS, PTFE) polymers by DFT calculations using the model molecules. *J Mol Struct.* 2016;1122:341-349. doi:10.1016/j.molstruc.2016.04.087
20. Triguero L, Plashkevych O, Pettersson LGM, Ågren H. Separate state vs. transition state Kohn-Sham calculations of X-ray photoelectron binding energies and chemical shifts. *J Electron Spectrosc Relat Phenomena.* 1999;104(1):195-207. doi:10.1016/S0368-2048(99)00008-0
21. Cavigliasso G, Chong DP. Accurate density-functional calculation of core-electron binding energies by a total-energy difference approach. *J Chem Phys.* 1999;111(21):9485-9492. doi:10.1063/1.480279
22. David Sherrill C, Schaefer HF. The configuration interaction method: Advances in highly correlated approaches. *Adv Quantum Chem.* 1999;34:143-269. doi:10.1016/S0065-3276(08)60532-8
23. Koopmans T. Ordering of wave functions and eigenenergies to the individual electrons of an atom. *Phys Ther.* 1933;1:104-113.
24. Bellafont NP, Illas F, Bagus PS. Validation of Koopmans' theorem for density functional theory binding energies. *Phys Chem Chem Phys.* 2015;17(6):4015-4019. doi:10.1039/c4cp05434b
25. Giesbers M, Marcelis ATM, Zuilhof H. Simulation of XPS C1s spectra of organic monolayers by quantum chemical methods. *Langmuir.* 2013;29(15):4782-4788. doi:10.1021/la400445s
26. Bagus PS, Sousa C, Illas F. Consequences of electron correlation for XPS binding energies: Representative case for C(1s) and O(1s) XPS of CO. *J Chem Phys.* 2016;145(14):144303. doi:10.1063/1.4964320
27. Tardio S, Cumpson PJ. Practical estimation of XPS binding energies using widely available quantum chemistry software. *Surf Interface Anal.* 2018;50(1):5-12. doi:10.1002/sia.6319
28. Kröner D, Ehlert C, Saalfrank P, Holländer A. Ab initio calculations for XPS chemical shifts of poly(vinyl-trifluoroacetate) using trimer models. *Surf Sci.* 2011;605(15-16):1516-1524. doi:10.1016/j.susc.2011.05.021
29. Baer DR, McGuire GE, Artyushkova K, Easton CD, Engelhard MH, Shard AG. Introduction to topical collection: Reproducibility challenges and solutions with a focus on guides to XPS analysis. *J Vac Sci Technol a.* 2021;39(2):021601. doi:10.1116/6.0000873
30. Major GH, Fairley N, Sherwood PMA, et al. Practical guide for curve fitting in x-ray photoelectron spectroscopy. *J Vac Sci Technol a.* 2020;38(6):061203. doi:10.1116/6.0000377
31. Nisol B, Reniers F. Challenges in the characterization of plasma polymers using XPS. *J Electron Spectrosc Relat Phenomena.* 2015;200:311-331. doi:10.1016/j.elspec.2015.05.002
32. Greczynski G, Hultman L. X-ray photoelectron spectroscopy: Towards reliable binding energy referencing. *Prog Mater Sci.* 2020;107:100591. doi:10.1016/j.pmatsci.2019.100591
33. Hanwell MD, Curtis DE, Lonie DC, Vandermeersch T, Zurek E, Hutchison GR. Avogadro: An advanced semantic chemical editor, visualization, and analysis platform. *J Chem.* 2012;4(1):17. doi:10.1186/1758-2946-4-17
34. Barca GMJ, Bertoni C, Carrington L, et al. Recent developments in the general atomic and molecular electronic structure system. *J Chem Phys.* 2020;152(15):154102. doi:10.1063/5.0005188
35. Pratt GW. Unrestricted Hartree-Fock method. *Phys Rev.* 1956;102(5):1303-1307. doi:10.1103/PhysRev.102.1303
36. Da Chai J, Head-Gordon M. Long-range corrected hybrid density functionals with damped atom-atom dispersion corrections. *Phys Chem Chem Phys.* 2008;10(44):6615-6620. doi:10.1039/b810189b
37. Tsuneda T, Hirao K. Self-interaction corrections in density functional theory. *J Chem Phys.* 2014;140(18):18A513. doi:10.1063/1.4866996
38. Grimme S, Steinmetz M. Effects of London dispersion correction in density functional theory on the structures of organic molecules in the gas phase. *Phys Chem Chem Phys.* 2013;15(38):16031-16042. doi:10.1039/c3cp52293h
39. Young DC. Spin contamination. In: Young DC, ed. *Computational chemistry.* John Wiley & Sons, Inc; 2003:227-230. doi:10.1002/0471220655.ch27.
40. Li CX. Active screen plasma nitriding – An overview. *Surf Eng.* 2010;26(1-2):135-141. doi:10.1179/174329409X439032
41. Biesinger MC. Polyethylene surfaces. 2015. <http://www.xpsfitting.com/2015/11/polyethylene-surfaces.html>
42. Paynter RW. XPS studies of the ageing of plasma-treated polymer surfaces. *Surf Interface Anal.* 2000;29(1):56-64. doi:10.1002/(SICI)1096-9918(200001)29:13.0.CO;2-2
43. Yasuda H. Plasma for modification of polymers. *J Macromol Sci Part a - Chem.* 1976;10(3):383-420. doi:10.1080/00222337608061190
44. Kauling AP, Soares GV, Figueroa CA, et al. Polypropylene surface modification by active screen plasma nitriding. *Mater Sci Eng C.* 2009;29(2):363-366. doi:10.1016/j.msec.2008.07.002
45. Grace JM, Zhuang HK, Gerenser LJ, Freeman DR. Time-resolved investigation of the surface chemical modification of poly(ethylene naphthalate) by nitrogen plasma treatment. *J Vac Sci Technol A.* 2003;21(1):37-46. doi:10.1116/1.1521960
46. Foerch R, Izawa J, Spears G. A comparative study of the effects of remote nitrogen plasma, remote oxygen plasma, and corona discharge

- treatments on the surface properties of polyethylene. *J Adhes Sci Technol*. 1991;5(7):549-564. doi:[10.1163/156856191X00747](https://doi.org/10.1163/156856191X00747)
47. Arumainayagam CR, Lee H-L, Nelson RB, Haines DR, Gunawardane RP. Low-energy electron-induced reactions in condensed matter. *Surf Sci Rep*. 2010;65(1):1-44. doi:[10.1016/j.surfrep.2009.09.001](https://doi.org/10.1016/j.surfrep.2009.09.001)
48. Li CX, Bell T. Potential of plasma nitriding of polymer for improved hardness and wear resistance. *J Mater Process Technol*. 2005;168(2):219-224. doi:[10.1016/j.jmatprotec.2004.10.018](https://doi.org/10.1016/j.jmatprotec.2004.10.018)
49. Kurtz SM. *The UHMWPE handbook: Ultra-high molecular weight polyethylene in total joint replacement*. Elsevier; 2004. doi:[10.1520/STP1445-EB](https://doi.org/10.1520/STP1445-EB).
50. Pippig F, Sarghini S, Holländer A, Paulussen S, Terryn H. TFAA chemical derivatization and XPS. Analysis of OH and NHx polymers. *Surf Interface Anal*. 2009;41(5):421-429. doi:[10.1002/sia.3043](https://doi.org/10.1002/sia.3043)
51. Taucher TC, Hehn I, Hofmann OT, Zharnikov M, Zojer E. Understanding chemical versus electrostatic shifts in X-ray photoelectron spectra of organic self-assembled monolayers. *J Phys Chem C*. 2016;120(6):3428-3437. doi:[10.1021/acs.jpcc.5b12387](https://doi.org/10.1021/acs.jpcc.5b12387)
52. Cabarcos OM, Shaporenko A, Weidner T, et al. Physical and electronic structure effects of embedded dipoles in self-assembled monolayers: Characterization of mid-chain ester functionalized alkanethiols on Au{111}. *J Phys Chem C*. 2008;112(29):10842-10854. doi:[10.1021/jp801618j](https://doi.org/10.1021/jp801618j)
53. Zhao J, Gao F, Pujari SP, Zuilhof H, Teplyakov AV. Universal calibration of computationally predicted N 1s binding energies for interpretation of XPS experimental measurements. *Langmuir*. 2017;33(41):10792-10799. doi:[10.1021/acs.langmuir.7b02301](https://doi.org/10.1021/acs.langmuir.7b02301)

## SUPPORTING INFORMATION

Additional supporting information may be found in the online version of the article at the publisher's website.

**How to cite this article:** Bruggeman M, Zelzer M, Dong H, Stamboulis A. Processing and interpretation of core-electron XPS spectra of complex plasma-treated polyethylene-based surfaces using a theoretical peak model. *Surf Interface Anal*. 2022;54(9):986-1007. doi:[10.1002/sia.7125](https://doi.org/10.1002/sia.7125)